Research Square

Preprints are preliminary reports that have not undergone peer review.
They should not be considered conclusive, used to inform clinical practice,
or referenced by the media as validated information.

Loganin Attenuates Postmenopausal Osteoporosis by Directly Targeting the RANK/RANKL Interface and Coordinating the Nrf2/HO-1 Antioxidant Axis with Energy Metabolism Reprogramming in Osteoclasts

Wei Deng

20201110040@stu.gzucm.edu.cn

Guangzhou University of Chinese Medicine https://orcid.org/0000-0002-1216-549X

Yongchao Tang

Guangzhou University of Chinese Medicine

Yihao Zhu

Guangzhou University of Chinese Medicine

Fanguo Kong

Henan luoyang guke yiyuan: Henan Luoyang Orthopedic Hospital

Shuncong Zhang

Guangzhou University of Chinese Medicine

Jiyao Luan

Henan luoyang guke yiyuan: Henan Luoyang Orthopedic Hospital

Research Article

Keywords: Loganin, Osteoclastogenesis, RANKL/RANK, Nrf2/HO-1, Energy metabolism, Postmenopausal osteoporosis

Posted Date: June 24th, 2026

DOI: https://doi.org/10.21203/rs.3.rs-9882780/v1

License: This work is licensed under a Creative Commons Attribution 4.0 International License.
Read Full License

Loganin Attenuates Postmenopausal Osteoporosis by Directly Targeting the RANK/RANKL Interface and Coordinating the Nrf2/HO-1 Antioxidant Axis with Energy Metabolism Reprogramming in Osteoclasts

Wei Deng2,3, Yongchao Tang2,3, Yihao Zhu2,3, Fanguo Kong1,*, Shuncong Zhang2,3,* Jiyao Luan1*,

1. Henan Luoyang Orthopedic Hospital (Henan Provincial Orthopedic Hospital), No. 100, Yongping Road, Zhengdong New District, Zhengzhou City, 450000, China;
2. The Laboratory of Orthopaedics and Traumatology of Lingnan Medical Research Center, Guangzhou University of Chinese Medicine, 12 Jichang Road, Baiyun District, Guangzhou 510405, China;
3. The First Affiliated Hospital of Guangzhou University of Chinese Medicine,No. 12, Airport Road, Baiyun District, Guangzhou City, Guangdong Province,510405, China;

***Corresponding authors:**

Jiyao Luan, Henan Luoyang Orthopedic Hospital (Henan Provincial Orthopedic Hospital), No. 100, Yongping Road, Zhengdong New District, Zhengzhou City, 450000, China. E-mail: wslw0814@126.com;

Shuncong Zhang, The Fist Affiliated Hospital of Guangzhou University of Chinese Medicine,No. 12, Airport Road, Baiyun District, Guangzhou City, Guangdong Province,510405, China.E-mail: zhangshuncong1479@gzucm.edu.cn

Fanguo Kong, Henan Luoyang Orthopedic Hospital (Henan Provincial Orthopedic Hospital), No. 100, Yongping Road, Zhengdong New District, Zhengzhou City, 450000, China. E-mail: Kongfanguo@126.com

Abstract:

Background: Postmenopausal osteoporosis (PMOP) is characterized by excessive osteoclast-mediated bone resorption driven by receptor activator of nuclear factor-κB ligand (RANKL) signaling. Loganin (LOG), an iridoid glycoside derived from *Cornus officinalis*, has demonstrated anti-inflammatory and antioxidant properties, yet its effects on osteoclastogenesis and the underlying mechanisms remain unclear.

Purpose: To investigate the inhibitory effects of LOG on RANKL-induced osteoclast differentiation and to elucidate the underlying molecular mechanisms in vitro and in vivo.

Methods: Bone marrow-derived macrophages (BMMs) were induced with M-CSF and RANKL to differentiate into osteoclasts with or without LOG co-treatment. Osteoclast formation was assessed by TRAP staining and F-actin ring immunofluorescence. Transcriptomic sequencing and targeted energy metabolomics were performed to identify core regulatory pathways. The Nrf2/Keap1/HO-1 antioxidant pathway, TRPV2/Ca^{2+}/CaMK IV calcium signaling axis, endoplasmic reticulum stress, mitochondrial function, AMPK/SIRT1/SIRT3–PGC-1α energy-sensing pathway, Wnt/β-catenin signaling, and cell migration were evaluated by Western blot, RT-qPCR, Seahorse metabolic flux analysis, and functional assays. Direct binding of LOG to RANK and RANKL was assessed by molecular docking, molecular dynamics simulation, surface plasmon resonance (SPR), and biolayer interferometry (BLI). An ovariectomized (OVX) mouse model was established to evaluate the therapeutic effects of LOG on bone microstructure, biomechanical properties, and antioxidant/anti-inflammatory responses in vivo.

Results: LOG dose-dependently inhibited RANKL-induced osteoclast differentiation and F-actin ring formation, predominantly during the early differentiation phase, without affecting BMM viability. LOG suppressed the expression of key osteoclastogenic markers (NFATc1, c-Fos, ACP5, and MMP9) at both mRNA and protein levels. Transcriptomic and metabolomic analyses revealed that LOG disrupted glycolysis–TCA cycle coupling and suppressed AMPK signaling pathway activity. Mechanistically, LOG activated the Nrf2/Keap1/HO-1 antioxidant pathway, attenuated intracellular and mitochondrial ROS accumulation, suppressed the TRPV2–Ca^{2+}–CaMK IV signaling axis, modulated endoplasmic reticulum stress, reduced mitochondrial membrane potential and ATP production, and downregulated the AMPK/SIRT1/SIRT3–PGC-1α pathway. LOG also inhibited osteoclast precursor migration by downregulating the CCL2/CCR2 axis, MMP2, and integrin β1, and suppressed Wnt/β-catenin signaling. SPR and BLI confirmed that LOG directly bound to both RANK ($K_D = 3.0 \times 10^{-8}$ M) and RANKL, with the capacity to interfere with the RANK–RANKL interaction interface. In OVX mice, LOG (10 $mg \cdot kg^{-1}$) significantly improved trabecular bone microstructure and biomechanical properties, reduced osteoclast numbers, activated the Nrf2/HO-1 pathway, and suppressed

inflammatory cytokines (IL-6 and TNF-α), achieving effects comparable to those of 17β-estradiol, without detectable organ toxicity.

Conclusion: LOG inhibits osteoclastogenesis through multi-target mechanisms involving direct interference with RANK–RANKL binding, activation of antioxidant defenses, suppression of calcium signaling and energy metabolism, and modulation of cell migration pathways. These findings identify LOG as a promising therapeutic candidate for PMOP.

Keywords:

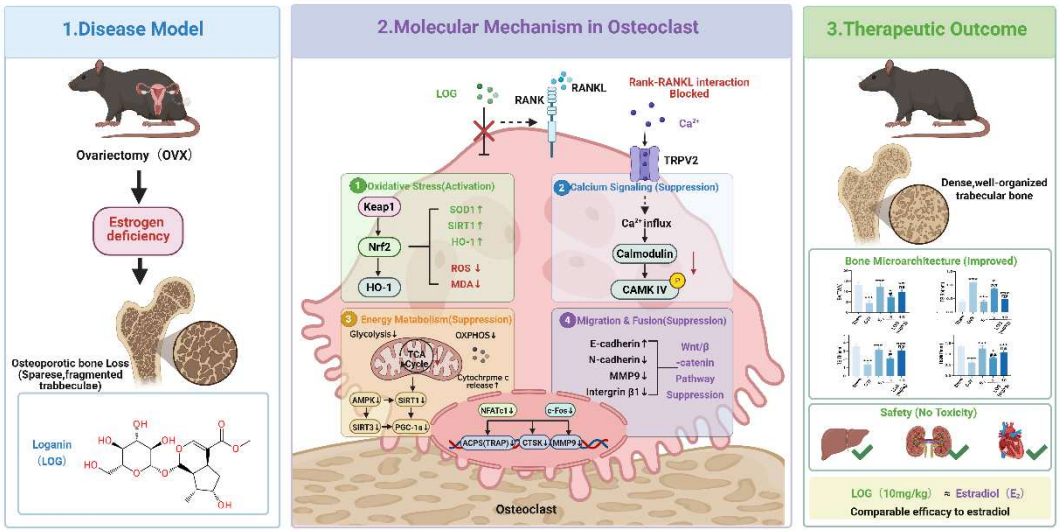
Loganin; Osteoclastogenesis; RANKL/RANK; Nrf2/HO-1; Energy metabolism; Postmenopausal osteoporosis

Abbreviation:

ACP5:Acid Phosphatase 5;ALT:Alanine Aminotransferase;AMPK:AMP-Activated Protein Kinase;AST: Aspartate Aminotransferase;ATF6:Activating Transcription Factor 6;BCA:Bicinchoninic Acid;BLI:Biolayer Interferometry;BMM:Bone Marrow-Derived Macrophage;BSA:Bovine Serum Albumin; BV/TV:Bone Volume;Fraction;CAT:Catalase;CCK-8:Cell Counting Kit-8;E_2:17β-Estradiol;ECAR:Extracellular Acidification Rate;ER:Endoplasmic Reticulum;FBS:Fetal Bovine Serum;GO:Gene Ontology;H&E:Hematoxylin and Eosin;HO-1:Heme Oxygenase 1;IHC:Immunohistochemistry;Keap1:Kelch-Like ECH-Associated Protein 1;KEGG:Kyoto Encyclopedia of Genes and Genomes;LOG:Loganin;M-CSF:Macrophage Colony-Stimulating Factor;NF-κB:Nuclear Factor κB;NFATc1:Nuclear Factor of Activated T Cells, Cytoplasmic 1;Nrf2:Nuclear Factor Erythroid 2-Related Factor 2;OCR:Oxygen Consumption Rate;OVX:Ovariectomy;PGC-1α: Peroxisome Proliferator-Activated Receptor Gamma Coactivator 1-Alpha ;Gamma:Coactivator 1-Alpha;PI:Propidium Iodide;RANKL:Receptor Activator of Nuclear Factor-κB Ligand;RMSF:Root-Mean-Square Fluctuation;ROI:Region of Interest;RT-qPCR:Quantitative Reverse Transcription PCR;SOD1:Superoxide Dismutase 1;SPR:Surface Plasmon Resonance;Tb.N:Trabecular Number;Tb.Sp:Trabecular Separation;Tb.Th:Trabecular Thickness;TRAP:Tartrate-Resistant Acid Phosphatase

Graphical Abstract:

Loganin (LOG) inhibits RANKL-induced osteoclast differentiation by directly targeting the RANKL/RANK signaling interface and coordinately regulating oxidative stress, calcium signaling, endoplasmic reticulum stress, mitochondrial function, and energy metabolism. LOG suppresses osteoclast marker expression, F-actin ring formation, and precursor migration in vitro, and alleviates OVX-induced bone loss and inflammation in vivo, indicating its therapeutic potential for postmenopausal osteoporosis.



1. Introduction

Postmenopausal osteoporosis (PMOP) is a systemic skeletal disorder characterized by progressive bone mass loss and microarchitectural deterioration following estrogen withdrawal, leading to increased fracture susceptibility(Compston et al., 2019; Salari et al., 2021) . The condition affects approximately 200 million women worldwide and constitutes a major public health burden due to the morbidity and mortality associated with osteoporotic fractures (Kanis et al., 2021). The fundamental pathological mechanism of PMOP involves an imbalance between bone formation and bone resorption, with excessive osteoclast activity being the predominant driver of bone loss (Chen et al., 2025). Current pharmacological interventions, including bisphosphonates, denosumab, and hormone replacement therapy, are effective but are associated with adverse effects such as osteonecrosis of the jaw, atypical fractures, and cardiovascular risks during long-term administration (Boyce and Xing, 2008; Flanigan et al., 2026; Zhou et al., 2026a). Therefore, the identification of novel therapeutic agents with favorable safety profiles that can effectively suppress pathological osteoclastogenesis remains an urgent clinical need.

Osteoclasts are multinucleated cells derived from the monocyte/macrophage lineage, and their differentiation is primarily governed by the receptor activator of nuclear factor-κB ligand (RANKL)/RANK signaling axis(Ono et al., 2020). Upon RANKL binding to RANK on osteoclast precursors, downstream cascades including nuclear factor of activated T cells cytoplasmic 1 (NFATc1), c-Fos, and nuclear factor-κB (NF-κB) are activated, driving the expression of osteoclast-specific genes such as tartrate-resistant acid phosphatase (TRAP) and matrix metalloproteinase 9 (MMP9) (Novotortsev et al., 2021; Park et al., 2017). Recent studies have revealed that osteoclast differentiation is accompanied by profound metabolic reprogramming, including enhanced mitochondrial oxidative phosphorylation, glycolysis, and reactive oxygen species (ROS) generation (Da et al., 2021; Lemma et al., 2016). Furthermore, calcium signaling mediated by transient receptor potential vanilloid (TRPV) channels and the calmodulin-dependent kinase (CaMK) cascade plays a critical role in NFATc1 nuclear translocation and osteoclast maturation(Tang et al., 2019) . These interconnected pathways represent potential multi-target therapeutic nodes for inhibiting osteoclastogenesis.

Loganin (LOG) is an iridoid glycoside predominantly found in *Cornus officinalis*, a traditional medicinal plant widely used in East Asian medicine for tonifying the liver and kidney (Deng et al., 2023). Accumulating pharmacological evidence has demonstrated that LOG possesses diverse biological activities, including anti-inflammatory, antioxidant, neuroprotective, and hepatoprotective effects(Dong et al., 2018; Liu et al., 2024). Recent investigations have shown that LOG can modulate NF-κB and mitogen-activated protein kinase (MAPK) signaling pathways and attenuate oxidative stress through activation of the nuclear factor erythroid 2-related factor 2 (Nrf2) pathway in various disease models (Chen et al., 2020; Zhou et al., 2026b). Notably, *Cornus officinalis* extracts have been reported to exert

osteoprotective effects in ovariectomized animal models (Misra et al., 2023). However, whether LOG, as a single active compound, can directly inhibit osteoclast differentiation and the precise molecular mechanisms involved remain largely unexplored.

In the present study, we systematically investigated the effects of LOG on RANKL-induced osteoclastogenesis using an integrated approach combining transcriptomics, targeted energy metabolomics, molecular docking, surface plasmon resonance, and in vivo validation in ovariectomized (OVX) mice. We aimed to elucidate the multi-target mechanisms by which LOG regulates osteoclast differentiation, encompassing direct RANK/RANKL binding interference, Nrf2/HO-1 antioxidant pathway activation, TRPV2/Ca^{2+}/CaMK IV signaling suppression, energy metabolism disruption, and cell migration inhibition. Our findings provide comprehensive mechanistic evidence supporting LOG as a promising therapeutic candidate for the treatment of postmenopausal osteoporosis.

2. Materials and Methods

2.1. Reagents and Drugs

Loganin (LOG, CAS: 18524-94-2; Chamface, Wuhan, China) was dissolved in dimethyl sulfoxide (DMSO) to prepare a stock solution and stored protected from light, then diluted in culture medium to the required working concentrations prior to use with the final DMSO concentration maintained at ≤0.1%; an equal volume of DMSO was added to all control groups as vehicle. 17β-Estradiol (E_2; Sigma-Aldrich, #E8875) was used as the positive control in vivo and diluted in physiological saline before administration. Macrophage colony-stimulating factor (M-CSF; PeproTech, #315-02) and receptor activator of nuclear factor-κB ligand (RANKL; R&D Systems, #462-TEC) were used to induce osteoclast differentiation.

2.2. Isolation and Culture of BMMs, Cell Viability Assay, and Osteoclast Differentiation

Bone marrow-derived macrophages (BMMs) were isolated from the femurs and tibias of 6-week-old male C57BL/6 mice under sterile conditions, with the marrow cavities flushed using α-Minimum Essential Medium (α-MEM; Gibco, #12571063). After filtration through a 200-mesh strainer, cells were resuspended in complete medium containing 10% fetal bovine serum (FBS; Gibco, #10099141), 1% penicillin-streptomycin (Gibco, #15140122), and 30 $ng \cdot mL^{-1}$ M-CSF, and incubated overnight at 37°C with 5% CO_2. Adherent cells collected the following day were used as BMMs.

For cytotoxicity assessment, BMMs were seeded into 96-well plates at 8×10^3 cells/well and treated with graded concentrations of LOG (0, 2.5, 5, 7.5, and 10 μM) for 48 h. Cell viability was determined using the Cell Counting Kit-8 (CCK-8;

Dojindo, #CK04). For osteoclast differentiation, BMMs were seeded at 1×10^4 cells/well in 96-well plates and cultured in induction medium containing 30 $ng \cdot mL^{-1}$ M-CSF and 50 $ng \cdot mL^{-1}$ RANKL, with the indicated LOG concentrations, for 7 days; medium was refreshed every two days. To identify the critical time window of LOG action, 10 μM LOG was applied at days 1–3, 3–5, 5–7, or 1–7. After fixation in 4% paraformaldehyde (PFA; Beyotime, #P0099), cells were stained using a tartrate-resistant acid phosphatase (TRAP) staining kit (Sigma-Aldrich, #387A-1KT), and TRAP-positive multinucleated cells (nuclei ≥ 3) were counted as mature osteoclasts. For each group, at least five randomly selected fields were counted independently by two blinded observers. For F-actin ring detection, BMMs were seeded at 5×10^3 cells/well in 96-well plates and cultured in osteoclast induction medium for 7 days, then fixed in 4% PFA. Cells were permeabilized with 0.1% Triton X-100 (Sigma-Aldrich, #T8787), blocked with 1% bovine serum albumin (BSA; Beyotime, #ST023), and incubated with tetramethylrhodamine isothiocyanate (TRITC)-labeled phalloidin (Abcam, #ab176756) at room temperature for 1 h in the dark, followed by 4',6-diamidino-2-phenylindole (DAPI; Beyotime, #C1002) counterstaining. F-actin ring area and nuclei per cell were quantified using ImageJ software.

2.3. Quantitative Reverse Transcription PCR (RT-qPCR) and Western Blot

Total RNA was extracted using TRIzol reagent (Invitrogen, #15596026). One microgram of RNA was reverse-transcribed using PrimeScript RT Master Mix (Takara, #RR036A), and quantitative amplification was performed with TB Green Premix Ex Taq II (Takara, #RR820A) on a CFX96 real-time PCR system (Bio-Rad). β-actin served as the internal reference for all RT-qPCR experiments, and relative expression was calculated using the 2^−ΔΔCt method.

For Western blot, all experiments were performed in three independent biological replicates (n = 3). Cells or femoral tissues (homogenized in liquid nitrogen) were lysed in radioimmunoprecipitation assay (RIPA) buffer (Beyotime, #P0013B) supplemented with protease and phosphatase inhibitors (Roche, #04693116001 and #04906845001). Nuclear and cytoplasmic proteins were isolated using a nuclear extraction kit (Beyotime, #P0028). Protein concentration was determined by bicinchoninic acid (BCA) assay (Thermo Fisher, #23225). Equal amounts of protein were separated by 10%–12% sodium dodecyl sulfate-polyacrylamide gel electrophoresis (SDS-PAGE; Epizyme, #PG112/PG113), transferred onto polyvinylidene difluoride (PVDF) membranes (Millipore, #IPVH00010), and blocked with 5% non-fat milk or 5% BSA for 1 h. β-actin served as the loading control for all Western blot experiments.

Detailed information on all primary antibodies, including target name, catalog number, host species, dilution, and application, is provided in Supplementary Table S1. Primary antibodies were diluted at 1:1000 (β-actin at 1:5000) and incubated overnight at 4°C. After washing with Tris-buffered saline with Tween-20 (TBST), membranes were incubated with horseradish peroxidase (HRP)-conjugated secondary

antibodies (CST, #7074/#7076, 1:5000) for 1 h at room temperature. Bands were visualized using enhanced chemiluminescence (ECL; Thermo, #34577) and quantified by ImageJ.

2.4. Transcriptomic Sequencing and Targeted Energy Metabolomics

Total RNA from the RANKL-induced group and the RANKL + LOG group (n = 3 per group) was assessed for integrity using an Agilent 2100 Bioanalyzer; libraries were then constructed and sequenced on the Illumina NovaSeq 6000 platform. After quality control, raw reads were aligned to the mouse reference genome, and differentially expressed genes (DEGs; $|\log_2$ fold change [FC]$| > 1$, $P < 0.05$) were identified using DESeq2. Functional annotation and pathway enrichment were performed using the Gene Ontology (GO) and Kyoto Encyclopedia of Genes and Genomes (KEGG) databases. Pathway activities for WNT, Estrogen, JAK-STAT, transforming growth factor β (TGFβ), nuclear factor κB (NF-κB), and tumor necrosis factor α (TNFα) were inferred using the Pathway RespOnsive GENes (PROGENy) algorithm.

For targeted metabolomics, BMMs induced with M-CSF and RANKL were treated with vehicle or 10 μM LOG (n = 4 per group). After washing with cold phosphate-buffered saline (PBS), cells were extracted with pre-cooled 80% methanol containing 0.1% formic acid at −80°C for 20 min, followed by repeated freeze-thaw cycles and sonication. Supernatants obtained after centrifugation (4°C, 14,000 × g, 15 min) were dried under nitrogen, reconstituted in 10% acetonitrile, and filtered through a 0.22 μm membrane. Chromatographic separation was performed on an ACQUITY UPLC BEH Amide column (Waters, #186004801) with gradient elution, and detection was carried out on an AB SCIEX QTRAP 6500+ system in multiple reaction monitoring (MRM) mode. Pooled quality control (QC) samples, prepared by combining equal aliquots from all experimental samples, were injected at regular intervals (every five analytical runs) throughout the sequence to monitor instrument stability and data reproducibility. Data were processed using MultiQuant 3.0.3 and normalized via internal standards. Orthogonal partial least squares discriminant analysis (OPLS-DA) models were constructed and validated by R^2Y, Q^2Y values, and 200-permutation tests to ensure model robustness. Differential metabolites were identified using variable importance in projection (VIP) > 1 from the OPLS-DA model, $|\log_2 FC| > 0.5$, and Student's t-test ($P < 0.05$). Annotation was based on the Human Metabolome Database (HMDB), and pathway enrichment was performed using KEGG (mmu) with differential abundance scores (DA-scores) to quantify pathway-level regulation.

2.5. Oxidative Stress, Calcium Signaling, and Cell Apoptosis Assays

Intracellular reactive oxygen species (ROS) were detected using the 2',7'-dichlorodihydrofluorescein diacetate (DCFH-DA) probe (Beyotime, #S0033); fluorescence images were captured using an Olympus IX73 fluorescence microscope and quantified by measuring mean fluorescence intensity using ImageJ software.

Mitochondrial ROS (mtROS) were assessed using MitoSOX Red (Invitrogen, #M36008) combined with DAPI counterstaining. Superoxide dismutase 1 (SOD1) activity, glutathione (GSH), and malondialdehyde (MDA) contents were measured using the respective kits (Beyotime, #S0101, #S0053, and #S0131S). Intracellular calcium (Ca^{2+}) levels were detected using the Fluo-4 AM probe (Invitrogen, #F14201), with fluorescence images captured using an Olympus IX73 microscope and quantified by ImageJ. To verify whether Ca^{2+} acted upstream of LOG, cells were pretreated with 10 μM LOG for 1 h and then stimulated with ionomycin (1 μM; Sigma-Aldrich, #I0634) for 30 min before phosphorylated calcium/calmodulin-dependent protein kinase IV (p-CaMK IV) detection. Apoptosis and membrane integrity were evaluated using a Hoechst 33342/propidium iodide (PI) double-staining kit (Beyotime, #C1056). Mitochondrial membrane potential ($\Delta\Psi m$) was assessed by tetramethylrhodamine methyl ester (TMRM; Invitrogen, #T668) combined with MitoTracker Green FM (MTG; Invitrogen, #M7514).

2.6. Real-Time Energy Metabolism Assay and Cell Migration

Oxygen consumption rate (OCR) and extracellular acidification rate (ECAR) were measured using the XF Cell Mito Stress Test Kit (Agilent, #103015-100) and XF Glycolysis Stress Test Kit (Agilent, #103020-100), respectively, on a Seahorse XFe96 Analyzer. Total ATP production rate and the relative contributions of mitochondrial ATP (mitoATP) and glycolytic ATP (glycoATP) were determined using the XF Real-Time ATP Rate Assay Kit (Agilent, #103592-100). Intracellular lactate, ATP, and ADP were quantified using the corresponding kits (Beyotime, #S0208, #S0026; Abcam, #ab83359), and citrate synthase activity was measured using the Citrate Synthase Activity Assay Kit (Sigma-Aldrich, #CS0720). Cell migration was evaluated by wound-healing assay: BMMs were seeded in 6-well plates and scratched at approximately 90% confluence using a 200 μL pipette tip. The medium was then replaced with osteoclast induction medium (OIM) containing graded LOG concentrations (0, 1.25, 2.5, 5, and 10 μM), and images of the scratched area were captured at 0, 12, 24, and 48 h. Wound widths were measured by ImageJ.

2.7. Molecular Docking, Molecular Dynamics Simulation, and SPR/BLI Validation

The crystal structures of RANK (PDB ID: 3ME4) and RANKL (PDB ID: 4GIQ) were obtained from the RCSB Protein Data Bank, and the LOG structure was downloaded from PubChem (CID: 87691) and converted into a three-dimensional structure using ChemDraw 20.0. Proteins and ligands were preprocessed (water removal, hydrogen addition, and Gasteiger charge calculation) using AutoDockTools 1.5.7 and saved in pdbqt format. Docking was performed with AutoDock Vina 1.2.3, and optimal poses were selected based on binding energy. Interactions were visualized using Discovery Studio 2019. The optimal docked complexes were subjected to 100 ns all-atom molecular dynamics (MD) simulations using GROMACS 2022.3, with proteins and ligands parameterized under the AMBER99SB-ILDN and General

AMBER Force Field (GAFF), respectively. Systems were solvated in a TIP3P water box, neutralized with Na^+/Cl^-, and equilibrated under NVT (100 ps, 310 K) and NPT (100 ps, 1 bar) ensembles before production simulation. Trajectory analyses generated ligand root-mean-square deviation (RMSD), complex RMSD, radius of gyration (Rg), solvent-accessible surface area (SASA), root-mean-square fluctuation (RMSF), and hydrogen bond counts. Gibbs free energy landscapes (FEL) were constructed based on RMSD-Rg projections, and binding free energies (ΔG_bind) were calculated using the g_mmpbsa tool.

For biophysical validation, binding kinetics between LOG and RANK or RANKL were assessed using a Biacore T200 surface plasmon resonance (SPR) system (Cytiva). His-tagged RANK (Sino Biological, #10519-H08H) and RANKL (Sino Biological, #11682-HNCH) were immobilized on NTA sensor chips (Cytiva, #BR100407), and graded concentrations of LOG (1.25–50 μM) were injected as the mobile phase. Response unit (RU) curves were recorded and fitted using BIAevaluation software to derive equilibrium dissociation constants (K_D). For the RANK/RANKL complex, biolayer interferometry (BLI) was performed on an Octet RED96 system (Sartorius), using Ni-NTA biosensors (Sartorius, #18-5101) to capture His-RANKL pre-incubated with RANK, followed by association-dissociation analysis with graded LOG concentrations.

2.8. OVX Mouse Model, Micro-CT Scanning, Biomechanical Testing, and Histological Evaluation

Six-week-old SPF female C57BL/6 mice were acclimatized for one week and randomly divided into five groups (n = 8 per group): Sham, OVX + Vehicle, OVX + E_2 (100 μg·kg^{-1}), OVX + LOG (5 mg·kg^{-1}), and OVX + LOG (10 mg·kg^{-1}). Mice were anesthetized with 2% isoflurane; Sham animals received removal of an equivalent volume of perigonadal adipose tissue, whereas the remaining groups underwent bilateral ovariectomy (OVX). Penicillin was administered postoperatively, and mice were allowed to recover for one week. From the second postoperative week onward, a therapeutic regimen was employed in which drug administration commenced after the initial phase of OVX-induced bone loss had been established. Mice received intraperitoneal injections every other day for eight weeks; the Sham and OVX + Vehicle groups received equal volumes of saline. At the end of the intervention, mice were deeply anesthetized and blood was collected via cardiac puncture for serum isolation. Bilateral femurs and lumbar vertebrae (L4–L5) were harvested; one side was fixed in 4% PFA for Micro-CT and histological analyses, while the other was snap-frozen for Western blot.

After 72 h fixation, samples were scanned on a Skyscan 1276 Micro-CT system (Bruker) at 70 kV, 200 μA, and 9 μm resolution. Reconstructed images (NRecon) were analyzed in CTAn, with the region of interest (ROI) defined as 100 continuous slices starting 0.5 mm below the distal femoral growth plate, to quantify bone volume fraction (BV/TV), trabecular number (Tb.N), trabecular thickness (Tb.Th), and

trabecular separation (Tb.Sp). Biomechanical testing was performed on the right femur using an Instron 5544 material testing machine in three-point bending mode (span 15 mm; loading rate 1 mm/min), yielding maximum load, elastic modulus, yield load, and energy to failure. For histology, femoral samples were decalcified in 10% ethylenediaminetetraacetic acid (EDTA; Solarbio, #E1171) for four weeks, dehydrated, embedded in paraffin, and cut into 5 μm sections for hematoxylin and eosin (H&E; Beyotime, #C0105S) and TRAP staining. Liver, kidney, lung, and heart sections were processed for H&E staining to assess organ histology. For nuclear factor erythroid 2-related factor 2 (Nrf2) immunohistochemistry (IHC), sections were incubated with anti-Nrf2 (Abcam, #ab62352, 1:200) overnight, followed by HRP-conjugated secondary antibody (CST, #7074, 1:500) for 1 h, and visualized using a 3,3'-diaminobenzidine (DAB) kit (Abcam, #ab64238). IHC scores were quantified using the IHC Profiler plugin in ImageJ. Serum levels of alanine aminotransferase (ALT), aspartate aminotransferase (AST), creatinine (CRE), and blood urea nitrogen (BUN) were measured using the corresponding kits (Nanjing Jiancheng, #C009-2-1, #C010-2-1, #C011-2-1, #C013-2-1). TRAP (Abcam, #ab230941), osteoprotegerin (OPG; Abcam, #ab203633), interleukin-6 (IL-6; Abcam, #ab234570), and tumor necrosis factor-α (TNF-α; Abcam, #ab236712) were measured by enzyme-linked immunosorbent assay (ELISA).

2.9. Statistical Analysis

Data are expressed as mean ± standard deviation (SD). Normality of data distribution was assessed using the Shapiro-Wilk test, and homogeneity of variances was evaluated using Levene's test. For data that satisfied the assumptions of normality and homoscedasticity, comparisons between two groups were performed using two-sided Student's t-test, while multi-group comparisons used one-way analysis of variance (ANOVA) followed by Tukey's post-hoc test. For datasets involving two independent variables (e.g., concentration and time), two-way ANOVA with Bonferroni's post-hoc test was applied. For data that did not satisfy the assumptions of parametric tests, non-parametric methods (Mann-Whitney U test for two-group comparisons or Kruskal-Wallis test followed by Dunn's post-hoc test for multi-group comparisons) were employed. All statistical analyses and graphs were performed in GraphPad Prism 9.0, with $P < 0.05$ considered statistically significant.

3. Results

3.1. LOG Inhibits RANKL-Induced Osteoclast Differentiation and F-Actin Ring Formation in a Dose-Dependent Manner

The chemical structure of Loganin (LOG) is shown in Fig. 1A. CCK-8 results (Fig. 1B) indicated that treatment with LOG at 0–10 μM for 48 h did not significantly affect BMM viability compared with the control group, confirming that this concentration range was free of overt cytotoxicity and could serve as the safe working

range for subsequent experiments.

After confirming the non-toxic dose range, the effect of LOG on RANKL-induced osteoclastogenesis was examined. TRAP staining (Fig. 1C) revealed that RANKL stimulation alone generated numerous large, deeply stained TRAP-positive multinucleated cells, whereas LOG co-treatment progressively reduced both osteoclast number and cell body area in a concentration-dependent manner. Quantitative analysis (Fig. 1D) confirmed that 2.5 μM LOG significantly decreased the number of TRAP-positive multinucleated cells (nuclei ≥ 3), with further enhancement at 5, 7.5, and 10 μM. To identify the critical time window of LOG action, 10 μM LOG was applied during the early (days 1–3), middle (days 3–5), late (days 5–7), or entire (days 1–7) phase of induction. Fig. 1E and F showed that early-phase treatment produced the most pronounced inhibition, comparable in magnitude to full-course treatment; middle-phase treatment resulted in only mild suppression, while late-phase treatment did not produce a statistically significant effect. These findings indicate that LOG acts predominantly during the early stage of osteoclast differentiation.

Given that the F-actin ring is a critical cytoskeletal structure required for bone-resorptive activity of mature osteoclasts, its formation was further assessed by immunofluorescence staining. Fig. 1G showed that RANKL stimulation alone produced intact, continuous F-actin rings encircling multiple nuclei, whereas LOG treatment led to progressive disassembly and shrinkage of these ring structures. Quantitative analysis (Fig. 1H and I) demonstrated that both the F-actin ring area per field and the number of nuclei per osteoclast were significantly reduced in the 5 and 10 μM LOG groups in a dose-dependent fashion. Collectively, these results demonstrate that LOG suppresses early osteoclast differentiation and multinuclear fusion without compromising BMM viability, accompanied by disruption of the F-actin ring architecture.

3.2. LOG Downregulates Key Osteoclast Differentiation Transcription Factors, and Transcriptomic Analysis Reveals Multi-Pathway Coordinated Regulation

Osteoclast formation depends on the expression of downstream genes driven by transcription factors such as NFATc1 and c-Fos. Having confirmed the phenotypic inhibitory effect of LOG, we next examined its molecular actions at both the transcriptional and translational levels. RT-qPCR results (Fig. 2A) showed that RANKL stimulation alone significantly upregulated the mRNA levels of *Acp5*, *Mmp9*, *Nfatc1*, and *Fos*, whereas LOG co-treatment dose-dependently suppressed these genes, with the most pronounced reduction observed in the 10 μM group. Western blot results (Fig. 2B) were consistent with these findings: c-Fos, MMP9, ACP5, and NFATc1 protein levels progressively accumulated following RANKL stimulation and peaked at day 5; LOG co-treatment significantly reduced the protein levels of all four markers at days 3 and 5 compared with the RANKL-only group (Fig.

2C).

To further elucidate the molecular basis underlying the inhibitory effects of LOG, transcriptomic sequencing was performed on the RANKL-induced group and the RANKL + LOG group. A hierarchical clustering heatmap (Fig. 2D) demonstrated clear segregation of the gene expression profiles between the two groups. The volcano plot (Fig. 2E) revealed a large number of DEGs, among which *Cxcl2*, *Acod1*, *Clec4e*, *Tnf*, *Ikbke*, and *Nfkbiz* were significantly upregulated. A chord diagram (Fig. 2F) and a Sankey diagram (Fig. 2G) of the DEGs indicated that these genes were predominantly associated with the immune system, signal transduction, and human disease-related functional modules. GO enrichment analysis (Fig. 2H) showed that the DEGs were mainly enriched in defense response, immune response, inflammatory response, cytokine production, and cytokine receptor binding terms. KEGG analysis (Fig. 2I) demonstrated significant enrichment in the TNF, NF-κB, and Janus kinase–signal transducer and activator of transcription (JAK-STAT) signaling pathways, as well as cytokine–cytokine receptor interaction and osteoclast differentiation pathways. A pathway activity heatmap (Fig. 2J) further revealed that the activities of the WNT, Estrogen, JAK-STAT, TGFβ, NF-κB, and TNFα pathways were markedly reduced in the LOG group. These results delineate the core signaling network regulated by LOG and provide a basis for subsequent mechanistic analyses.

3.3. LOG Disrupts Glycolysis–TCA Cycle Coupling and Energy Metabolism Homeostasis in Osteoclasts

Having established that energy metabolism and signal transduction pathways were among the core modules identified by transcriptomic analysis, targeted energy metabolomics was employed to characterize the specific metabolic alterations. Fig. 3A showed that the metabolite profiles of the RANKL-induced group and the RANKL + LOG group exhibited clear clustering separation: several glycolytic intermediates (glucose 1-phosphate, glucose 6-phosphate, fructose 6-phosphate, and 6-phosphogluconate) and key tricarboxylic acid (TCA) cycle metabolites (cis-aconitate, fumarate, malate, glutamate, and trans-aconitate) were significantly downregulated following LOG treatment, whereas acetyl-CoA showed an opposite upward trend. Combined $\log_2$(FC) and VIP analysis (Fig. 3B) confirmed that most downregulated metabolites had VIP values greater than 1, indicating substantial discriminatory contribution to group separation. A Pearson correlation matrix (Fig. 3C) revealed significant positive correlations among the downregulated TCA cycle and glycolytic intermediates, reflecting a coordinated suppressive effect of LOG on this metabolic axis. Violin plots of seven representative differential metabolites (Fig. 3D) further validated these trends: acetyl-CoA was significantly accumulated in the LOG group, while 6-phosphogluconate, cis-aconitate, fumarate, malate, glutamate, and trans-aconitate were significantly reduced. Notably, upstream accumulation of acetyl-CoA was accompanied by depletion of downstream TCA intermediates.

Circos diagrams (Fig. 3E and 3H) illustrated the topological connections of

differential metabolites among the TCA cycle, glycolysis, and amino acid metabolism pathways. KEGG pathway enrichment analysis (Fig. 3F) showed that the differential metabolites were significantly enriched in the TCA cycle, central carbon metabolism in cancer, glycolysis/gluconeogenesis, pyruvate metabolism, glyoxylate and dicarboxylate metabolism, the pentose phosphate pathway, and oxidative phosphorylation, with DA-scores generally deviating from zero, indicating significant alterations in pathway activity. A Sankey diagram (Fig. 3G) showed that the differential metabolites were primarily assigned to carbohydrate metabolism, energy metabolism, amino acid metabolism, and signal transduction within the KEGG primary classification. A bubble plot (Fig. 3I) showed that the AMP-activated protein kinase (AMPK) signaling pathway (mmu04152), central carbon metabolism in cancer (mmu05230), TCA cycle (mmu00020), glycolysis/gluconeogenesis (mmu00010), glyoxylate and dicarboxylate metabolism (mmu00630), and pyruvate metabolism (mmu00620) exhibited the highest enrichment. A circular pathway activity plot (Fig. 3J) further demonstrated that energy metabolism-related pathways, including AMPK, hypoxia-inducible factor 1 (HIF-1), TCA cycle, and oxidative phosphorylation (OXPHOS), showed a coordinated downregulation trend following LOG treatment. Taken together, these results indicate that LOG disrupts energy metabolism homeostasis required for osteoclast differentiation by suppressing glycolysis–TCA cycle coupling and AMPK signaling pathway activity.

3.4. LOG Activates the Nrf2/Keap1/HO-1 Antioxidant Pathway and Alleviates RANKL-Induced Oxidative Stress

Transcriptomic analysis indicated that oxidation–inflammation-related pathways constituted one of the core modules of LOG action; therefore, validation was first performed at the level of oxidative stress. Western blot results (Fig. 4A) showed that, compared with the Control group, stimulation with RANKL alone significantly downregulated the protein levels of total Nrf2, nuclear Nrf2, heme oxygenase-1 (HO-1), SOD1, and catalase (CAT), while Kelch-like ECH-associated protein 1 (Keap1) expression was upregulated, indicating suppression of the antioxidant defense system during osteoclast differentiation. With increasing LOG concentrations (2.5, 5, and 10 μM), the above antioxidant proteins were restored in a dose-dependent manner, whereas Keap1 levels decreased correspondingly. Quantitative analysis (Fig. 4B–F) confirmed that the levels of total Nrf2, nuclear Nrf2, HO-1, SOD1, and CAT in the 10 μM LOG group were significantly higher than those in the RANKL group.

At the level of reactive oxygen species (ROS) production and antioxidant enzyme activity, DCFH-DA fluorescence staining showed that RANKL stimulation markedly elevated intracellular ROS levels, and the green fluorescence intensity was attenuated in a dose-dependent manner following LOG treatment (Fig. 4G). Quantitative results (Fig. 4H and 4I) indicated that ROS levels in the LOG-treated groups were significantly lower than those in the RANKL group. SOD1 activity (Fig. 4J) and GSH content (Fig. 4K) were decreased after RANKL stimulation and progressively recovered upon LOG co-treatment, with the 10 μM group approaching

Control levels. These results indicate that LOG activates the Nrf2/Keap1/HO-1 antioxidant pathway and enhances SOD1 activity and GSH levels, thereby alleviating RANKL-induced oxidative stress.

3.5. LOG Suppresses the TRPV2–Ca^{2+}–CaMK IV Calcium Signaling Axis

After confirming the regulatory effect of LOG on oxidative stress, its influence on calcium signaling was further examined. Western blot results (Fig. 4L) showed that phosphorylated calmodulin (p-Calmodulin), p-CaMK IV, and transient receptor potential vanilloid 2 (TRPV2) were maintained at relatively high levels at each time point (0–60 min) under RANKL stimulation. Co-treatment with LOG (10 μM) resulted in an overall reduction in the phosphorylation or expression levels of these proteins. In contrast, no appreciable difference in phosphorylated calcium/calmodulin-dependent protein kinase II (p-CaMK II) was observed between the two groups (Fig. 4O). Quantitative analysis showed that LOG significantly reduced the phosphorylation level of p-CaMK IV across all examined time points (0–60 min; Fig. 4N) and downregulated TRPV2 protein expression (Fig. 4P). p-Calmodulin was significantly decreased at the early time points (0–15 min) but showed a partial recovery at 60 min (Fig. 4M), displaying a time-dependent dynamic pattern.

To determine whether Ca^{2+} acts upstream of LOG-mediated signaling, an ionomycin rescue experiment was performed. As shown in Fig. 4Q and 4R, LOG (10 μM) treatment alone significantly reduced p-CaMK IV levels, whereas the addition of the Ca^{2+} ionophore ionomycin markedly reversed this inhibitory effect, suggesting that the suppression of CaMK IV by LOG is at least partially mediated through regulation of intracellular Ca^{2+} concentration. Fluo-4 AM fluorescence staining (Fig. 4S) showed that RANKL stimulation significantly increased intracellular Ca^{2+} levels, and green fluorescence was attenuated in a dose-dependent manner following LOG treatment. Quantitative results (Fig. 4T) confirmed that the Ca^{2+} level in the 10 μM LOG group was significantly lower than that in the RANKL group. Together, these data indicate that LOG suppresses TRPV2-mediated Ca^{2+} influx and downregulates Calmodulin–CaMK IV signaling axis activity, thereby inhibiting early calcium signal transduction during osteoclast differentiation.

3.6. LOG Modulates RANKL-Induced Endoplasmic Reticulum Stress Response and Mitochondrial Function

After confirming the regulatory effects of LOG on oxidative stress and calcium signaling, its influence on endoplasmic reticulum (ER) stress and mitochondrial function was further investigated. Western blot results (Fig. 5A) showed that, compared with the RANKL-only group, LOG co-treatment led to differential changes in ER stress-related proteins. Calnexin levels were significantly elevated at all examined time points (0, 15, 30, 45, and 60 min) following LOG treatment (Fig. 5B), suggesting a possible enhancement of ER protein folding quality control. Glucose-regulated protein 78 (GRP78) was significantly reduced at the 30 min and 60 min time points, whereas no significant difference was observed at 45 min (Fig. 5C),

indicating that the activation of the unfolded protein response (UPR) was partially suppressed. Endoplasmic reticulum oxidoreductase 1-like (ERO1L) showed no significant difference between the two groups (Fig. 5D), suggesting that the effect of LOG on ER oxidative folding was limited. The pro-apoptotic branch effector DNA damage-inducible transcript 3/C/EBP homologous protein (DDIT3/CHOP) was significantly decreased at 0, 15, and 30 min under LOG treatment and remained at relatively low levels at 45 and 60 min (Fig. 5E). Inositol-requiring enzyme 1 (IRE1) showed a similar downward trend (Fig. 5G). Activating transcription factor 6 (ATF6) was significantly upregulated at the 45 and 60 min time points following LOG treatment (Fig. 5F), suggesting that LOG exerts differential regulatory effects on distinct UPR branches (IRE1, ATF6, and protein kinase R-like ER kinase [PERK]/CHOP).

Hoechst 33342/PI dual staining (Fig. 5H) showed that with increasing LOG concentrations, the proportion of PI-positive cells increased, and the PI/Hoechst 33342 ratio was elevated in a dose-dependent manner (Fig. 5I). Notably, this observation appeared to contrast with the CCK-8 results, which confirmed that LOG at the concentrations used did not exert cytotoxicity on BMMs. MitoSOX Red fluorescence staining (Fig. 5J) showed that red fluorescence intensity was markedly attenuated after LOG treatment (Fig. 5K), indicating reduced mtROS generation. TMRM/MTG dual staining (Fig. 5L) revealed that TMRM red fluorescence was significantly decreased, and the TMRM/MTG ratio declined in a dose-dependent manner (Fig. 5M) indicating a reduction in mitochondrial membrane potential. At the level of energy metabolism, Seahorse real-time flux analysis (Fig. 5N and 5O) showed that RANKL stimulation significantly increased the OCR and ECAR of BMMs. Both parameters decreased in a dose-dependent manner upon LOG co-treatment, with the high-dose group approaching Control levels, suggesting that LOG suppressed the enhancement of mitochondrial oxidative phosphorylation and glycolysis during osteoclast differentiation.

3.7. LOG Suppresses ATP Production, TCA Cycle Activity, and the AMPK/SIRT1/SIRT3–PGC-1α Energy-Sensing Pathway in Osteoclasts

After confirming the regulatory effects of LOG on ER stress and mitochondrial membrane potential (Section 3.6), its role was further examined at the levels of energy supply and mitochondrial functional proteins. Seahorse real-time detection results (Fig. 6A) showed that the total adenosine triphosphate (ATP) production rate of BMMs was significantly elevated after RANKL stimulation compared with the Control group, and this rate decreased in a dose-dependent manner with increasing LOG concentrations (2.5, 5, and 10 μM). Fig. 6B further resolved the relative contributions of mitoATP (blue) and glycoATP (green). Both showed a declining trend following LOG treatment, suggesting coordinated suppression of mitochondrial oxidative phosphorylation and glycolytic energy supply. Consistent with these changes in energy metabolism, intracellular lactate levels were significantly elevated under RANKL stimulation (Fig. 6C) and decreased in a dose-dependent manner after

LOG treatment. The ATP/adenosine diphosphate (ADP) ratio was significantly increased in the RANKL group (Fig. 6D) and progressively declined following LOG treatment, with a corresponding increase in ADP levels (Fig. 6E). Citrate synthase activity was significantly elevated in the RANKL group (Fig. 6F) and decreased in a dose-dependent manner after LOG treatment, indicating suppression of the TCA cycle entry enzyme activity.

To further verify mitochondrial function and upstream energy-sensing pathway responses at the protein level, Western blot analysis was performed. As shown in Fig. 6G–L, using whole-cell lysates, the total protein level of cytochrome c (Cyt c) was increased in a dose-dependent manner following LOG treatment (Fig. 6H). Cytochrome c oxidase subunit IV (COX IV) was significantly upregulated after RANKL stimulation and significantly downregulated upon LOG treatment (Fig. 6L), indicating suppression of respiratory chain complex IV protein expression. Succinate dehydrogenase complex flavoprotein subunit A (SDHA) and prohibitin 1 (PHB1) showed no significant differences among groups (Fig. 6I and 6J), suggesting that LOG selectively affects distinct mitochondrial functional modules. Heat shock protein 60 (HSP60) showed a declining trend after LOG treatment but did not reach statistical significance (Fig. 6K).

At the level of energy-sensing pathways (Fig. 6M), sirtuin 1 (SIRT1) (Fig. 6N), sirtuin 3 (SIRT3) (Fig. 6O), and the phosphorylated AMPK (p-AMPK)/AMPK ratio (Fig. 6Q) were all significantly upregulated under RANKL stimulation and decreased in a dose-dependent manner following LOG treatment. Peroxisome proliferator-activated receptor gamma coactivator 1-alpha (PGC-1α) was significantly downregulated at the low LOG concentration (2.5 μM), whereas a gradual recovery trend was observed at 5 and 10 μM (Fig. 6P), displaying a non-monotonic concentration–response relationship. These results indicate that LOG suppresses the AMPK/SIRT1/SIRT3–PGC-1α energy-sensing pathway, downregulates key mitochondrial oxidative phosphorylation proteins, and elevates total Cyt c protein levels, thereby restricting the mitochondrial function and energy supply required for osteoclast differentiation.

3.8. LOG Directly Binds to RANK and RANKL and Interferes with the RANK–RANKL Interaction Interface

After confirming the regulatory effects of LOG on multiple downstream signaling pathways, whether LOG directly targets the core initiating signal of osteoclast differentiation, RANK/RANKL, was further investigated through molecular docking, MD simulation, and biophysical experiments.

Static docking analysis. Molecular docking results (Fig. 7A) showed that LOG was accommodated within the active pocket of RANK, forming conventional hydrogen bonds with key amino acid residues including LYS A:384 and ASN A:350, along with non-covalent interactions with surrounding hydrophobic and polar residues. Fig. 7B showed that the binding interface between LOG and RANKL was

more extensive, involving key residues such as LYS 244, HIS 253, and ARG 264, with multiple types of non-covalent interactions including hydrogen bonds, carbon–hydrogen bonds, van der Waals forces, and alkyl interactions.

Dynamic stability verification. A 100 ns all-atom MD simulation was performed based on the optimal docking conformation to evaluate the dynamic stability of the complexes. Ligand RMSD analysis (Fig. 7C) showed that the ligand RMSD of the RANKL–LOG complex was maintained at approximately 0.10 nm throughout the simulation, whereas that of the RANK–LOG complex exhibited notable fluctuations at approximately 20 ns and 80 ns, suggesting that the LOG conformation was more convergent within the RANKL binding pocket. Analyses of the Rg (Fig. 7D), SASA (Fig. 7E), and hydrogen bond number (Fig. 7H) showed that both complexes exhibited no apparent drift during the simulation and consistently maintained 2–6 stable hydrogen bonds, indicating that the hydrogen bond network is an important factor in sustaining binding stability. Complex RMSD analysis (Fig. 7F) showed that the RANK–LOG complex was maintained at approximately 0.20 nm, while the RANKL–LOG complex remained within the range of 0.45–0.60 nm, with a higher fluctuation amplitude than the RANK–LOG complex. RMSF analysis (Fig. 7G) showed that residue fluctuations in the core structural regions of both complexes were concentrated within 0.1–0.3 nm, with local peaks observed only at the terminal and loop regions. The FEL (Fig. 7I and 7J) showed that both complexes exhibited a single global energy minimum basin in the RMSD–Rg two-dimensional space, indicating that the complexes converged to the dominant conformational state within the simulation time frame.

Binding free energy quantification. Molecular mechanics Poisson–Boltzmann surface area (MM-PBSA) binding free energy analysis (Fig. 7K) showed that the ΔG_bind of the RANKL–LOG complex was –23.00 kcal/mol, compared with –19.83 kcal/mol for the RANK–LOG complex. Van der Waals forces and electrostatic interactions were the major favorable contributing terms for both complexes, and the more negative overall ΔG_bind of the RANKL–LOG complex suggests a relatively higher binding affinity.

Experimental validation. SPR results (Fig. 7L) showed that the binding response of LOG (1.25–50 μM) to immobilized RANK was dose-dependent, with a response value of approximately 47 RU at 50 μM. The equilibrium dissociation constant (K_D) was determined to be 3.0×10^{-8} M, confirming a direct and specific interaction between LOG and RANK. The SPR response of LOG to RANKL (Fig. 7M) also increased in a concentration-dependent manner, reaching approximately 48 RU at 50 μM, although dissociation was relatively faster. BLI results (Fig. 7N) showed that when RANK and RANKL were pre-assembled as a complex, the binding response of LOG was markedly enhanced, reaching approximately 87 nm shift at 50 μM, with the association–dissociation curves displaying rapid on/off kinetic characteristics.

Taken together, both the computational and experimental evidence indicate that

LOG possesses direct binding capacity toward both RANK and RANKL, with RANKL being the target with higher binding affinity. LOG can simultaneously occupy the RANK–RANKL interaction interface and may influence the initiation of downstream osteoclast differentiation signaling by interfering with the RANK–RANKL interaction.

3.9. LOG Suppresses Osteoclast Precursor Migration and Adhesion-Related Molecule Expression and Interferes with the Wnt/β-Catenin Signaling Pathway

After confirming the regulatory effects of LOG on signal transduction and energy metabolism, its influence on osteoclast precursor migration and related molecular expression was further examined.Wound healing assay results (Fig. 8A) showed that under OIM stimulation, the scratch area in the 0 μM LOG group progressively closed at 12, 24, and 48 h. With increasing LOG concentrations (1.25, 2.5, 5, and 10 μM), the rate of wound closure was markedly reduced, and the scratch width in the 10 μM group remained close to the initial level at 48 h. Quantitative results (Fig. 8B) confirmed that the maintenance of scratch width by LOG was dose- and time-dependent.

At the level of cell adhesion-related molecules, Western blot results (Fig. 8C) showed that E-cadherin protein levels decreased in a dose-dependent manner with increasing LOG concentrations, while N-cadherin showed a corresponding increasing trend. Quantitative analysis (Fig. 8D) confirmed that the N-cadherin/β-actin ratio was significantly elevated, whereas the E-cadherin/β-actin ratio was significantly reduced.

Western blot results (Fig. 8E) showed that matrix metalloproteinase 2 (MMP2), C-C motif chemokine ligand 2 (CCL2), C-C motif chemokine receptor 2 (CCR2), and integrin β1 protein levels were all downregulated in a dose-dependent manner following LOG treatment. Quantitative results (Fig. 8F) showed that the expression levels of these proteins were significantly decreased compared with the 0 μM group. RT-qPCR results (Fig. 8G) were consistent with the protein-level findings, showing that the mRNA levels of *Ccl2*, *Mmp2*, *Ccr2*, and *Itgb1* were all significantly decreased in a dose-dependent manner upon LOG treatment. These results suggest that the inhibition of osteoclast precursor migration by LOG is primarily mediated through downregulation of the CCL2/CCR2 chemotactic signaling axis and matrix degradation- and adhesion-related molecules including MMP2 and integrin β1.

Given the involvement of the Wnt/β-catenin signaling pathway in regulating cell migration and adhesion, its temporal response was further analyzed. Western blot results (Fig. 8H) showed that β-catenin protein levels in the RANKL-only group gradually declined over time, and this declining trend was further enhanced upon LOG co-treatment. Wnt3a remained relatively stable in the RANKL group but was notably reduced at 30, 45, and 60 min under LOG treatment. Quantitative results (Fig. 8I) showed that the β-catenin/β-actin ratio in the LOG co-treatment group was significantly lower than that in the RANKL group at all examined time points (0–60 min), and the Wnt3a/β-actin ratio was significantly downregulated at 30, 45, and 60

min. These results indicate that LOG suppresses the Wnt/β-catenin pathway activity and downregulates chemotactic and adhesion signaling molecules (CCL2/CCR2, MMP2, and integrin β1), thereby coordinately restricting the migration and fusion of osteoclast precursors.

3.10. LOG Improves Bone Microstructure, Bone Metabolic Markers, and Biomechanical Properties in OVX Mice

To verify the osteoprotective effects of LOG in vivo, an OVX model was established using female C57BL/6 mice (6–8 weeks old) to evaluate the effects of LOG on postmenopausal osteoporosis (PMOP). As shown in the experimental design (Fig. 9A), mice were divided into the Sham group, OVX + Vehicle group, OVX + E_2 group (100 μg·kg^{-1}), and OVX + LOG groups (5 and 10 mg·kg^{-1}). Detailed experimental procedures are described in the Materials and Methods section.

Micro-computed tomography (micro-CT) two-dimensional (2D) sagittal and three-dimensional (3D) reconstruction images of the distal femur (Fig. 9B) showed that, compared with the Sham group, the OVX group exhibited markedly sparse trabecular structure with evident trabecular fracture and loss. E_2 treatment significantly restored bone microstructure, and LOG treatment led to a dose-dependent recovery of trabecular number and connectivity, with the 10 mg·kg^{-1} LOG group approaching the level observed in the E_2 group. Quantitative analysis (Fig. 9C) further confirmed that BV/TV, Tb.Th, and Tb.N in the OVX group were significantly lower than those in the Sham group, while Tb.Sp was significantly higher. Following LOG treatment, BV/TV, Tb.Th, and Tb.N were restored in a dose-dependent manner, and Tb.Sp was significantly decreased. No statistically significant difference was detected between the 10 mg·kg^{-1} LOG group and the E_2 group for any of the above parameters.

At the lumbar vertebral level, 2D and 3D reconstruction images (Fig. 9D) showed that the OVX group displayed markedly sparse vertebral trabeculae (red arrows indicate areas of bone loss). Following LOG treatment, trabecular density within the vertebral body was progressively restored, and the morphological appearance of the 10 mg·kg^{-1} group was comparable to that of the Sham group. Quantitative results (Fig. 9E) showed that vertebral BV/TV, Tb.N, and Tb.Th in the OVX group were significantly decreased, while Tb.Sp was significantly increased. All parameters showed dose-dependent improvement following LOG treatment, and no statistically significant difference was detected between the 10 mg·kg^{-1} LOG group and the E_2 group.

Regarding serum bone metabolic markers, Fig. 9F showed that serum TRAP levels in the OVX group were significantly higher than those in the Sham group, and TRAP levels decreased in a dose-dependent manner following LOG treatment, with the 10 mg·kg^{-1} group approaching Sham levels. Fig. 9G showed that serum OPG levels in the OVX group were significantly lower than those in the Sham group, and OPG levels were significantly restored following E_2 and LOG treatment.

Biomechanical testing results (Fig. 9H) showed that the maximum load, elastic modulus, yield load, and energy to failure of the femur in the OVX group were all significantly decreased compared with the Sham group. These biomechanical parameters were restored in a dose-dependent manner following LOG treatment, with no statistically significant difference detected between the 10 $mg \cdot kg^{-1}$ LOG group and the E_2 group. These results indicate that LOG dose-dependently alleviates OVX-induced bone loss, improves bone microstructure, and enhances biomechanical properties in vivo, with the osteoprotective effects of the 10 $mg \cdot kg^{-1}$ LOG group being comparable to those of the E_2 group.

3.11. LOG Improves Trabecular Bone Morphology, Suppresses Osteoclast Marker Protein Expression, and Demonstrates Favorable In Vivo Safety in OVX Mice

Building upon the micro-CT and biomechanical assessments (Section 3.10), the in vivo effects of LOG were further evaluated at the histological, protein expression, and safety levels.H&E staining of the distal femur (Fig. 10A) showed that the Sham group displayed intact trabecular structure, whereas the OVX group exhibited markedly sparse and fragmented trabeculae with enlarged bone marrow cavities. E_2 treatment significantly improved these pathological changes. LOG treatment led to a dose-dependent recovery of trabecular structure, with the trabecular density in the 10 $mg \cdot kg^{-1}$ group approaching that of the E_2 group. Histomorphometric quantitative results were consistent with these observations. BV/TV (Fig. 10B) and bone surface (BS, Fig. 10C) in the OVX group were significantly lower than those in the Sham group. In the 10 $mg \cdot kg^{-1}$ LOG group, both parameters were significantly restored compared with the OVX group, with no statistically significant difference detected relative to the E_2 group. The 5 $mg \cdot kg^{-1}$ LOG group showed partial improvement compared with the OVX group but remained significantly different from the E_2 group.

TRAP staining results (Fig. 10D) showed that numerous TRAP-positive multinucleated osteoclasts were present along the trabecular bone surface in the OVX group, and the number of positive cells was markedly reduced following E_2 and LOG treatment. Quantitative analysis showed that osteoclast number/bone surface (N.Oc/BS, Fig. 10E) and osteoclast surface/bone surface (Oc.S/BS, Fig. 10F) in the OVX group were significantly higher than those in the Sham group. In the 10 $mg \cdot kg^{-1}$ LOG group, both N.Oc/BS and Oc.S/BS were significantly decreased, with no statistically significant difference detected compared with the E_2 group. In the 5 $mg \cdot kg^{-1}$ LOG group, N.Oc/BS and Oc.S/BS were significantly lower than those in the OVX group, but both parameters remained significantly different from the E_2 group.

The inhibitory effect of LOG on the osteoclast differentiation pathway in vivo was further verified at the protein expression level. Western blot results (Fig. 10O) showed that the protein expression levels of ACP5, MMP9, NFATc1, and c-Fos in femoral tissue were markedly upregulated in the OVX group compared with the Sham group, and were decreased in a dose-dependent manner following E_2 and LOG

treatment. Quantitative analysis (Fig. 10P–S) confirmed that the ACP5/β-actin (Fig. 10P), MMP9/β-actin (Fig. 10Q), NFATc1/β-actin (Fig. 10R), and c-Fos/β-actin (Fig. 10S) ratios in the OVX group were all significantly elevated compared with the Sham group. In the 10 mg·kg^{-1} LOG group, all of the above ratios were significantly reduced, with no statistically significant difference detected compared with the E_2 group. In the 5 mg·kg^{-1} LOG group, all protein ratios were significantly decreased compared with the OVX group but remained significantly different from the E_2 group.

In addition, histopathological examination and serum biochemical analysis of major organs were performed to evaluate the in vivo safety of long-term LOG administration. H&E staining of the liver (Fig. 10G), lungs (Fig. 10H), kidneys (Fig. 10I), and heart (Fig. 10J) showed no apparent inflammatory cell infiltration, degenerative necrosis, or fibrosis in any group, and tissue architecture was comparable to that of the Sham group. Serum levels of ALT (Fig. 10K), AST (Fig. 10L), CRE (Fig. 10M), and BUN (Fig. 10N) showed no statistically significant differences among groups, indicating that LOG at the doses used in this study did not cause detectable hepatic or renal injury or systemic toxicity.

Taken together, these results indicate that LOG dose-dependently improves trabecular bone microstructure, reduces osteoclast number and bone resorption surface area, and downregulates key osteoclast-related proteins (ACP5, MMP9, NFATc1, and c-Fos) in OVX mice, without causing apparent organ toxicity or hepatic and renal functional abnormalities.

3.12. LOG Activates the Nrf2/HO-1 Antioxidant Pathway and Suppresses Inflammatory Responses In Vivo

Building upon the histological and safety assessments (Section 3.11), the in vivo effects of LOG were further evaluated at the levels of antioxidant pathway activation and inflammation.IHC staining for Nrf2 in the distal femur (Fig. 11A) showed that the Sham group displayed widely distributed Nrf2-positive signals in the trabecular bone region, whereas positive expression was markedly diminished in the OVX group. E_2 treatment significantly upregulated Nrf2-positive signals, and LOG treatment led to a dose-dependent recovery of Nrf2 expression, with staining intensity in the 10 mg·kg^{-1} group being comparable to that in the E_2 group. Quantitative IHC scoring results (Fig. 11B) confirmed that the Nrf2 IHC score in the OVX group was significantly lower than that in the Sham group **.** The scores in the E_2 and 10 mg·kg^{-1} LOG groups were significantly higher than those in the OVX group **.** The 5 mg·kg^{-1} LOG group showed partial recovery compared with the OVX group but remained below the Sham level.

At the level of oxidative stress indicators in femoral tissue homogenates (Fig. 11C–I), the levels of CAT, SOD1, Nrf2, and GSH in the OVX group were significantly decreased compared with the Sham group, while Keap1 and MDA levels were significantly elevated. ROS levels, measured using an oxidative stress detection kit for tissue homogenates, were significantly higher in the OVX group than in the Sham group. Following LOG treatment, the above indicators were restored in a dose-

dependent manner. In the 10 mg·kg⁻¹ LOG group, CAT, SOD1, Nrf2, and GSH levels were significantly higher than those in the OVX group, while Keap1, ROS, and MDA levels were significantly decreased, with no statistically significant differences detected compared with the E_2 group. At the level of inflammatory indicators, Fig. 11J and 11K showed that IL-6 and TNF-α levels in femoral tissue homogenates of the OVX group were significantly elevated compared with the Sham group. Both inflammatory factors decreased in a dose-dependent manner following LOG treatment, with the 10 mg·kg⁻¹ LOG group approaching Sham levels and showing no statistically significant difference detected compared with the E_2 group.

At the protein expression level, Western blot results (Fig. 11L) showed that the protein expression levels of CAT, HO-1, Nrf2, and SOD1 in femoral tissue were markedly downregulated in the OVX group compared with the Sham group and were restored in a dose-dependent manner following E_2 and LOG treatment, with band densities in the 10 mg·kg⁻¹ LOG group being comparable to those in the E_2 group. Quantitative analysis (Fig. 11M) confirmed that the CAT/β-actin, HO-1/β-actin, Nrf2/β-actin, and SOD1/β-actin ratios in the OVX group were significantly decreased compared with the Sham group . In the 10 mg·kg⁻¹ LOG group, the above ratios were significantly restored, with no statistically significant differences detected compared with the E_2 group. The 5 mg·kg⁻¹ LOG group showed partial improvement in certain indicators (such as Nrf2 and SOD1), but the effects were less pronounced than those in the 10 mg·kg⁻¹ group.

These results indicate that LOG dose-dependently activates the Nrf2/HO-1 antioxidant pathway in vivo, elevates antioxidant enzyme levels including CAT and SOD1, reduces ROS and MDA accumulation, and suppresses the levels of inflammatory factors IL-6 and TNF-α, thereby ameliorating OVX-induced oxidative stress and the inflammatory microenvironment.

4. Discussion

The present study provides comprehensive evidence that LOG inhibits RANKL-induced osteoclastogenesis through a multi-target mechanism encompassing direct RANK/RANKL binding interference, antioxidant pathway activation, calcium signaling suppression, energy metabolism disruption, and migration inhibition. Our finding that LOG directly binds to both RANK and RANKL, confirmed by SPR ($K_D = 3.0 \times 10^{-8}$ M) and BLI, represents a novel mechanism by which a natural iridoid glycoside interferes with the initiating signal of osteoclast differentiation. Previous studies have demonstrated that disrupting the RANK–RANKL protein-protein interaction is an effective strategy for suppressing osteoclastogenesis (Wang et al., 2022; Xu et al., 2025; Zhao et al., 2026). The computational analyses further revealed that the RANKL–LOG complex exhibited lower binding free energy (–23.00 kcal/mol) and more stable ligand conformational convergence than the RANK–LOG complex, suggesting preferential binding to RANKL. This direct targeting

mechanism, combined with the downstream multi-pathway regulation, distinguishes LOG from conventional single-target anti-resorptive agents and supports its potential as a multi-modal therapeutic candidate.

A key mechanistic finding of this study is the activation of the Nrf2/Keap1/HO-1 antioxidant axis by LOG, which effectively counteracted RANKL-induced oxidative stress both in vitro and in vivo. Oxidative stress plays a pivotal role in driving osteoclast differentiation, as ROS serve as essential second messengers downstream of RANKL signaling (Sun et al., 2021; Zhang et al., 2021). Our results demonstrated that LOG dose-dependently restored Nrf2 nuclear translocation, upregulated HO-1, SOD1, and CAT expression, and reduced intracellular and mitochondrial ROS levels. Simultaneously, LOG suppressed the TRPV2–Ca^{2+}–CaMK IV signaling axis, and the ionomycin rescue experiment confirmed that this effect was mediated through regulation of intracellular Ca^{2+} concentration. The interplay between ROS and calcium signaling in osteoclasts has been increasingly recognized, with ROS promoting Ca^{2+} release and amplifying NFATc1 activation (Green et al., 2021; Ren et al., 2022). Our data suggest that LOG may interrupt this positive feedback loop by simultaneously targeting both arms, thereby achieving synergistic inhibition of early osteoclast commitment.

The metabolomic and bioenergetic analyses revealed that LOG profoundly disrupted the metabolic reprogramming required for osteoclast differentiation. The accumulation of acetyl-CoA accompanied by depletion of downstream TCA cycle intermediates suggests that LOG may block the conversion of acetyl-CoA to citrate, thereby restricting overall TCA flux. This interpretation is consistent with the observed reduction in citrate synthase activity. Furthermore, LOG suppressed both mitochondrial oxidative phosphorylation and glycolysis, reduced ATP production, and downregulated the AMPK/SIRT1/SIRT3–PGC-1α energy-sensing pathway. The non-monotonic response of PGC-1α, which was suppressed at low concentrations but partially recovered at higher doses, may reflect a compensatory mitochondrial biogenesis response triggered by severe energy depletion (Da et al., 2021; Park-Min, 2019). Additionally, the increase in total Cyt c protein detected in whole-cell lysates may indicate enhanced mitochondrial membrane permeability; however, definitive confirmation of Cyt c redistribution requires subcellular fractionation experiments, which represents a limitation of the current study(Li et al., 2025).

Regarding the in vivo relevance, LOG at 10 $mg \cdot kg^{-1}$ achieved therapeutic effects comparable to those of E_2 in OVX mice, including improved bone microstructure, enhanced biomechanical properties, and reduced osteoclast numbers, without detectable hepatic or renal toxicity. The discrepancy between CCK-8 viability results and Hoechst 33342/PI staining observed in vitro likely reflects that LOG selectively promotes death of differentiating osteoclast precursors under RANKL stimulation rather than exerting direct cytotoxicity on undifferentiated BMMs, consistent with differentiation-dependent cell fate determination (McDonald et al., 2021). The reduction of E-cadherin observed in the migration experiments may reflect decreased

fusion capacity of osteoclast precursors rather than enhanced epithelial-mesenchymal transition, given that E-cadherin mediates cell-cell fusion in the monocyte-macrophage lineage(Pereira et al., 2018). Collectively, our findings establish LOG as a promising multi-target therapeutic agent for PMOP. Future studies should investigate the pharmacokinetic profile and long-term safety of LOG, and explore its potential synergistic effects with existing anti-osteoporosis medications in clinical settings (Lee et al., 2022; Long et al., 2022).

Ethical Approval and Consent to Participate

All animal experiments were conducted in accordance with the Guidelines for the Care and Use of Laboratory Animals issued by the Chinese National Ministry of Science and Technology and approved by the Animal Ethics Committee of Guangzhou University of Chinese Medicine (approval number: 20260519016).

Consent for publication

All authors have read and approved the final version of the manuscript and consent to its publication in *Phytomedicine*.

Availability of data and material

The data that support the findings of this study are available from the corresponding author upon reasonable request.

Author contributions

Wei Deng: Conceptualization, Methodology, Investigation, Formal analysis, Writing – original draft, Writing – review & editing. **Yongchao Tang:** Investigation, Validation, Formal analysis.**Yihao Zhu:** Investigation, Methodology, Validation, Software. **Shuncong Zhang:** Resources, Supervision, Project administration, Writing – review & editing. **Fanguo Kong:** Conceptualization, Supervision, Funding acquisition, Writing – review & editing. **Jiyao Luan:** Conceptualization, Supervision, Project administration, Funding acquisition, Writing – review & editing.All authors have read and approved the final version of the manuscript.

Acknowledgments

None.

Competing Interest

The authors declare that they have no known competing financial interests or personal relationships that could have appeared to influence the work reported in this paper.

Supplementary materials

Supplementary Table S1. Detailed information of primary antibodies used in this study.

Supplementary Table S2. Primer sequences used for RT-qPCR.

Funding information:

Basic and Applied Basic Research Fund Natural Science Foundation in Guangdong Province, China (Number: 2026A1515012042); Henan Provincial Special Research Project on Traditional Chinese Medicine (Grant Nos. 20-21ZY1058 and 20-21ZY2243); Luoyang Municipal Special Project for Medical and Health in the Public

Welfare Sector (Grant No. 2022008A).

Figure Legends

Fig. 1. LOG inhibits RANKL-induced osteoclast differentiation and F-actin ring formation in a dose-dependent manner. (A) Chemical structure of LOG. (B) Cell viability of BMMs treated with the indicated concentrations of LOG (0, 2.5, 5, 7.5, and 10 μM) for 48 h, assessed by CCK-8 assay. (C) Representative TRAP staining images of BMMs cultured with RANKL and the indicated concentrations of LOG for 7 days; lower panels show magnified views of the boxed areas. (D) Quantification of TRAP-positive multinucleated osteoclasts (nuclei ≥ 3). (E) Representative TRAP staining images following treatment with 10 μM LOG during different time windows (days 1–3, 3–5, 5–7, and 1–7). (F) Quantification of TRAP-positive multinucleated osteoclasts under the indicated time-window treatments. (G) Representative immunofluorescence images of F-actin rings (red, phalloidin) and nuclei (blue, DAPI) in osteoclasts treated with 0, 5, and 10 μM LOG. (H) Quantification of F-actin ring area per field. (I) Quantification of nuclei number per osteoclast. Data are presented as mean ± SD. *P < 0.05, **P < 0.01, ***P < 0.001; ns, not significant.

Fig. 2. LOG suppresses RANKL-induced osteoclast differentiation-related gene and protein expression and regulates multiple key signaling pathways. (A) RT-qPCR analysis of the mRNA expression levels of *Acp5*, *Mmp9*, *Nfatc1*, and *Fos* following treatment with RANKL alone or in combination with 5 or 10 μM LOG. (B) Western blot analysis of c-Fos, MMP9, ACP5, and NFATc1 protein expression at days 0, 1, 3, and 5 under RANKL stimulation alone or combined with 10 μM LOG; β-actin served as the loading control. (C) Densitometric quantification of each protein band normalized to β-actin. (D) Hierarchical clustering heatmap of DEGs between the RANKL-induced group and the RANKL + LOG group. (E) Volcano plot of DEGs; red dots indicate upregulated genes and blue dots indicate downregulated genes. (F) Chord diagram illustrating the associations among DEGs. (G) Sankey diagram showing the mapping of DEGs to KEGG pathways and functional categories. (H) GO enrichment analysis of DEGs across the three domains: biological process, cellular component, and molecular function. (I) KEGG pathway enrichment analysis. (J) Pathway activity heatmap of WNT, Estrogen, JAK-STAT, TGFβ, NF-κB, and TNFα signaling pathways, calculated using the PROGENy algorithm. Data are presented as mean ± SD. *P < 0.05, **P < 0.01, ***P < 0.001.

Fig. 3. Effects of LOG on glycolysis–TCA cycle coupling and energy metabolism pathways in osteoclasts. (A) Heatmap showing differential abundance of key glycolytic and TCA cycle metabolites between the RANKL-induced group and

the RANKL + LOG group. (B) Combined log_2(FC) and VIP analysis of differential metabolites. (C) Pearson correlation matrix among differential metabolites. (D) Violin plots of seven representative differential metabolites between the two groups. (E, H) Circos diagrams illustrating the topological associations of differential metabolites across the TCA cycle, glycolysis, and amino acid metabolism pathways. (F) KEGG pathway enrichment analysis (DA-score). (G) Sankey diagram depicting the hierarchical mapping of differential metabolites to KEGG pathways and functional categories. (I) KEGG pathway enrichment bubble plot. (J) Circular pathway activity plot showing overall trends of energy metabolism-related pathways. Data are presented as mean ± SD. *P < 0.05, **P < 0.01.

Figure 4. LOG alleviates RANKL-induced oxidative stress and calcium signaling activation by activating the Nrf2/Keap1 antioxidant pathway and suppressing the TRPV2/Ca^{2+}/CaMK IV signaling pathway. (A) Western blot analysis of total Nrf2, nuclear Nrf2, Keap1, HO-1, SOD1, and CAT protein expression levels following treatment with LOG at different concentrations (2.5, 5, and 10 μM). (B–F) Quantitative analysis of the above protein expression levels. (G) Intracellular ROS levels detected by DCFH-DA fluorescence staining. Scale bar = 50 μm. (H, I) Quantitative analysis of ROS fluorescence intensity. (J) Measurement of SOD1 enzymatic activity. (K) Measurement of intracellular GSH content. (L) Western blot analysis of p-Calmodulin 1/2/3, p-CaMK II, p-CaMK IV, and TRPV2 protein expression levels at different time points (0, 5, 15, 30, and 60 min). (M–P) Quantitative analysis of the above protein expression levels. (Q) Western blot analysis of p-CaMK IV expression changes in the ionomycin rescue experiment. (R) Quantitative analysis of p-CaMK IV. (S) Intracellular Ca^{2+} levels detected by Fluo-4 AM fluorescence staining. Scale bar = 50 μm. (T) Quantitative analysis of Ca^{2+} fluorescence intensity. Data are presented as mean ± SD. *P < 0.05, **P < 0.01, ***P < 0.001.

Figure 5. LOG modulates endoplasmic reticulum stress response and mitochondrial function during RANKL-induced osteoclast differentiation. (A) Western blot analysis of Calnexin, GRP78, ERO1L, DDIT3/CHOP, ATF6, and IRE1 protein expression levels at different time points (0, 15, 30, 45, and 60 min). (B–G) Quantitative analysis of the above protein expression levels. (H) Hoechst 33342/PI dual staining for cell death detection following treatment with LOG at different concentrations (2.5, 5, and 10 μM). Scale bar = 50 μm. (I) Quantitative analysis of the PI/Hoechst 33342 ratio. (J) MitoSOX Red fluorescence staining for detection of mtROS levels. Scale bar = 50 μm. (K) Quantitative analysis of mtROS fluorescence intensity. (L) TMRM/MTG dual staining for detection of mitochondrial membrane potential. Scale bar = 50 μm. (M) Quantitative analysis of the TMRM/MTG ratio. (N, O) Seahorse real-time flux analysis for measurement of the OCR and ECAR. Data are presented as mean ± SD. *P < 0.05, **P < 0.01, ***P < 0.001.

Figure 6. LOG suppresses ATP production, TCA cycle activity, and the AMPK/SIRT1/SIRT3–PGC-1α energy-sensing pathway in osteoclasts. (A) Total

ATP production rate of BMMs treated with LOG at different concentrations (0, 2.5, 5, and 10 μM) as measured by Seahorse real-time detection. (B) Analysis of the relative contributions of mitoATP (blue) and glycoATP (green). (C) Measurement of intracellular lactate levels. (D) Quantitative analysis of the ATP/ADP ratio. (E) Measurement of ADP levels. (F) Detection of citrate synthase activity. (G) Western blot analysis of Cyt c, SDHA, PHB1, HSP60, and COX IV protein expression levels; β-actin served as the loading control. (H–L) Quantitative analysis of the above protein expression levels: Cyt c/β-actin (H), SDHA/β-actin (I), PHB1/β-actin (J), HSP60/β-actin (K), and COX IV/β-actin (L) ratios. (M) Western blot analysis of SIRT1, SIRT3, PGC-1α, p-AMPK, and AMPK protein expression levels; β-actin served as the loading control. (N–Q) Quantitative analysis of the above protein expression levels: SIRT1/β-actin (N), SIRT3/β-actin (O), PGC-1α/β-actin (P), and p-AMPK/AMPK (Q) ratios. Data are presented as mean ± SD. *P < 0.05, **P < 0.01, ***P < 0.001.

Figure 7. Molecular docking, molecular dynamics simulation, and SPR/BLI binding kinetics validation of LOG with RANK and RANKL. (A) Molecular docking results of LOG with RANK, showing the 3D binding mode within the binding pocket and the 2D interaction diagram. (B) 3D binding mode and 2D interaction diagram of LOG with RANKL. (C) Ligand RMSD curves of the RANK–LOG and RANKL–LOG complexes during the 100 ns MD simulation. (D) Rg curves of the complexes over simulation time. (E) SASA curves of the complexes over simulation time. (F) Complex RMSD curves over simulation time. (G) RMSF analysis of RANK–LOG (red) and RANKL–LOG (Chain A/B, green/cyan). (H) Number of hydrogen bonds in the complexes over simulation time. (I, J) FEL two-dimensional projection maps based on RMSD–Rg for the RANK–LOG (I) and RANKL–LOG (J) complexes. (K) Binding free energy decomposition of the RANK–LOG and RANKL–LOG complexes calculated by the MM-PBSA method, including the van der Waals energy (ΔE_vdW), electrostatic energy (ΔE_elec), polar solvation energy (ΔG_polar), non-polar solvation energy (ΔG_nonpolar), and total binding free energy (ΔG_bind) components. (L) SPR real-time association–dissociation kinetic curves of LOG at different concentrations (1.25, 2.5, 5, 10, 20, and 50 μM) with immobilized RANK. (M) SPR real-time association–dissociation kinetic curves of LOG at different concentrations with immobilized RANKL. (N) BLI real-time association–dissociation kinetic curves of LOG at different concentrations with the pre-assembled RANK/RANKL complex.

Figure 8. LOG suppresses osteoclast precursor migration and Wnt/β-catenin signaling pathway activity. (A) Wound healing assay evaluating the migratory capacity of BMMs treated with LOG at different concentrations (0, 1.25, 2.5, 5, and 10 μM) at 0, 12, 24, and 48 h. (B) Quantitative analysis of scratch width. (C) Western blot analysis of E-cadherin and N-cadherin protein expression levels; β-actin served as the loading control. (D) Quantitative analysis of E-cadherin/β-actin and N-cadherin/β-actin ratios. (E) Western blot analysis of MMP2, CCL2, CCR2, and integrin β1 protein expression levels; β-actin served as the loading control. (F)

Quantitative analysis of the above protein expression levels. (G) RT-qPCR analysis of *Ccl2*, *Mmp2*, *Ccr2*, and *Itgb1* mRNA expression levels. (H) Western blot analysis of β-catenin and Wnt3a protein expression levels following stimulation with RANKL alone or co-treatment with RANKL and 10 μM LOG at different time points (0, 15, 30, 45, and 60 min); β-actin served as the loading control. (I) Quantitative analysis of β-catenin/β-actin and Wnt3a/β-actin ratios. Data are presented as mean ± SD. *P < 0.05, **P < 0.01, ***P < 0.001. NS indicates no statistical significance.

Figure 9. LOG improves femoral and lumbar vertebral bone microstructure, bone metabolic markers, and biomechanical properties in OVX mice. (A) Schematic illustration of the animal experimental design. Female C57BL/6 mice (6–8 weeks old) underwent OVX surgery to establish a PMOP model and were divided into the Sham group, OVX + Vehicle group, OVX + E_2 group (100 $\mu g \cdot kg^{-1}$), and OVX + LOG groups (5 and 10 $mg \cdot kg^{-1}$). (B) Micro-CT 2D sagittal images and 3D reconstruction images of the distal femur in each group. Scale bar = 2 mm. (C) Quantitative analysis of femoral bone microstructural parameters, including BV/TV, Tb.Sp, Tb.Th, and Tb.N. (D) Micro-CT 2D and 3D reconstruction images of lumbar vertebrae in each group; red arrows indicate areas of bone loss. Scale bar: 2 mm for 2D images, 5 mm for 3D images. (E) Quantitative analysis of lumbar vertebral bone microstructural parameters (BV/TV, Tb.N, Tb.Sp, and Tb.Th). (F) Serum TRAP levels measured by ELISA. (G) Serum OPG levels measured by ELISA. (H) Femoral biomechanical properties, including maximum load, elastic modulus, yield load, and energy to failure. Data are presented as mean ± SD. Compared with the OVX group: *P < 0.05, **P < 0.01, ***P < 0.001. Compared with the E_2 group: #P < 0.05, ##P < 0.01, ###P < 0.001. NS indicates no statistically significant difference compared with the E_2 group.

Figure 10. LOG improves trabecular bone morphology, suppresses osteoclast marker protein expression, and demonstrates favorable in vivo safety in OVX mice. (A) Representative H&E staining images of the distal femur in each group (original magnification: 5× and 10×). (B, C) Histomorphometric quantitative analysis of BV/TV (B) and BS (C). (D) Representative TRAP staining images of the distal femur in each group (original magnification: 5× and 10×). (E, F) Quantitative analysis of TRAP staining: N.Oc/BS (E) and Oc.S/BS (F). (G–J) Representative H&E staining images of major organs in each group: liver (G), lungs (H), kidneys (I), and heart (J). (K–N) Serum biochemical parameters: ALT (K), AST (L), CRE (M), and BUN (N). (O) Western blot analysis of ACP5, MMP9, NFATc1, and c-Fos protein expression levels in femoral tissue of each group; β-actin served as the loading control. (P–S) Quantitative analysis of the above protein expression levels: ACP5/β-actin (P), MMP9/β-actin (Q), NFATc1/β-actin (R), and c-Fos/β-actin (S) ratios. Data are presented as mean ± SD. Compared with the OVX group: *P < 0.05, **P < 0.01, ***P < 0.001. Compared with the E_2 group: #P < 0.05, ##P < 0.01. NS indicates no statistically significant difference compared with the E_2 group.

Figure 11. LOG activates the Nrf2/HO-1 antioxidant pathway and

suppresses OVX-induced inflammatory responses in vivo. (A) Representative IHC staining images of Nrf2 in the distal femur of each group (original magnification: 5× and 10×). (B) Quantitative analysis of Nrf2 IHC scores. (C–I) Detection of oxidative stress-related indicators in femoral tissue homogenates: CAT (C), Keap1 (D), ROS (E), SOD1 (F), Nrf2 (G), MDA (H), and GSH (I). (J, K) Detection of inflammatory factors in femoral tissue homogenates: IL-6 (J) and TNF-α (K). (L) Western blot analysis of CAT, HO-1, Nrf2, and SOD1 protein expression levels in femoral tissue of each group; β-actin served as the loading control. (M) Quantitative analysis of the above protein expression levels (CAT/β-actin, HO-1/β-actin, Nrf2/β-actin, and SOD1/β-actin ratios). Data are presented as mean ± SD. Compared with the OVX group: *$P < 0.05$, **$P < 0.01$, ***$P < 0.001$. Compared with the E_2 group: #$P < 0.05$, ##$P < 0.01$, ###$P < 0.001$. NS indicates no statistically significant difference compared with the E_2 group.

1217

1218

1219

1220

Figure 1 :

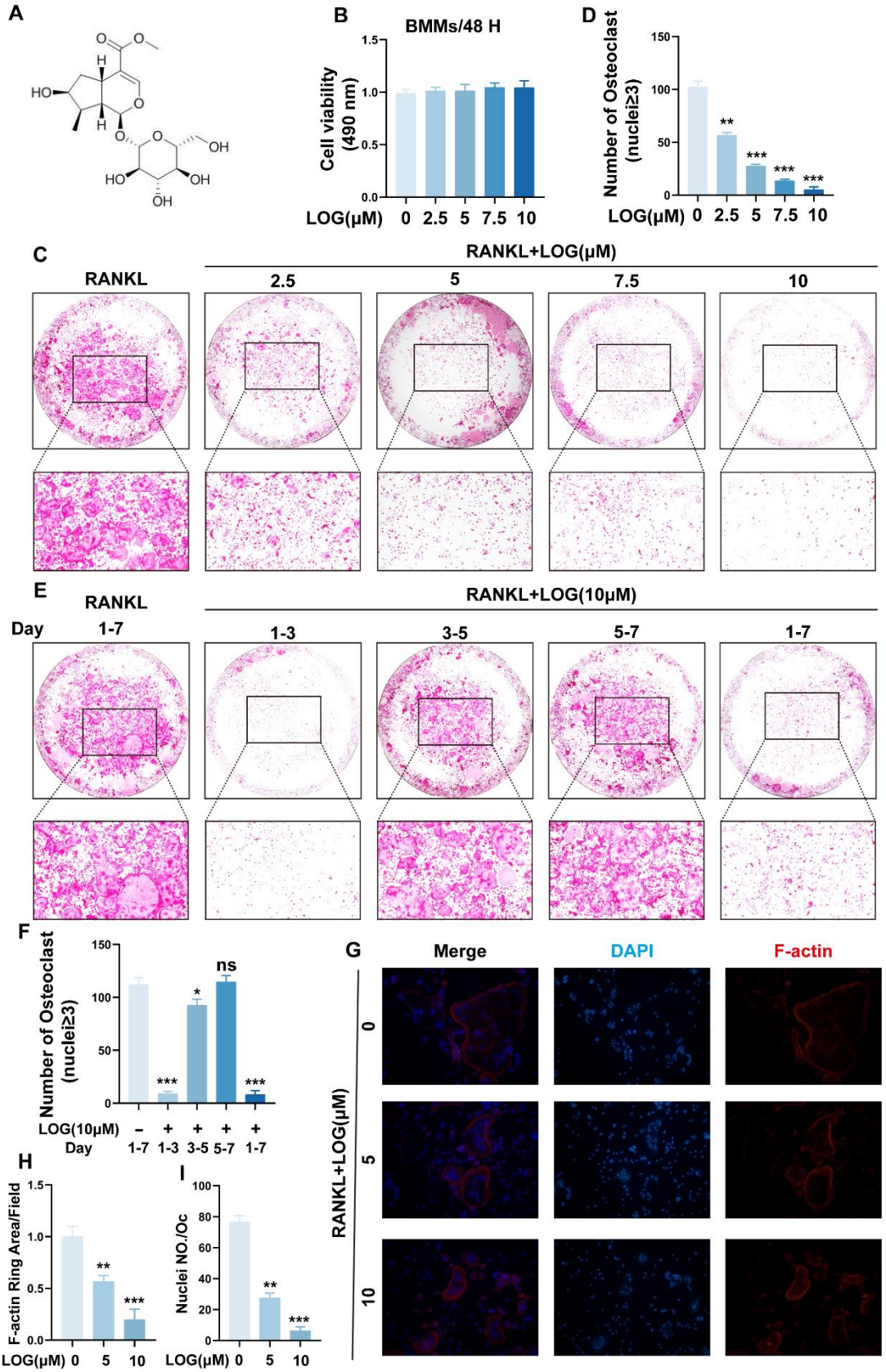

A
B
BMMs/48 H
Cell viability (490 nm)
LOG(μM) 0 2.5 5 7.5 10
D
Number of Osteoclast (nuclei≥3)
LOG(μM) 0 2.5 5 7.5 10
C
RANKL
RANKL+LOG(μM)
2.5
5
7.5
10
E
RANKL
RANKL+LOG(10μM)
Day
1-7
1-3
3-5
5-7
1-7
F
Number of Osteoclast (nuclei≥3)
ns
LOG(10μM) – + + + +
Day 1-7 1-3 3-5 5-7 1-7
G
Merge
DAPI
F-actin
RANKL+LOG(μM)
0
5
10
H
F-actin Ring Area/Field
LOG(μM) 0 5 10
I
Nuclei NO./Oc
LOG(μM) 0 5 10

Figure 2 :

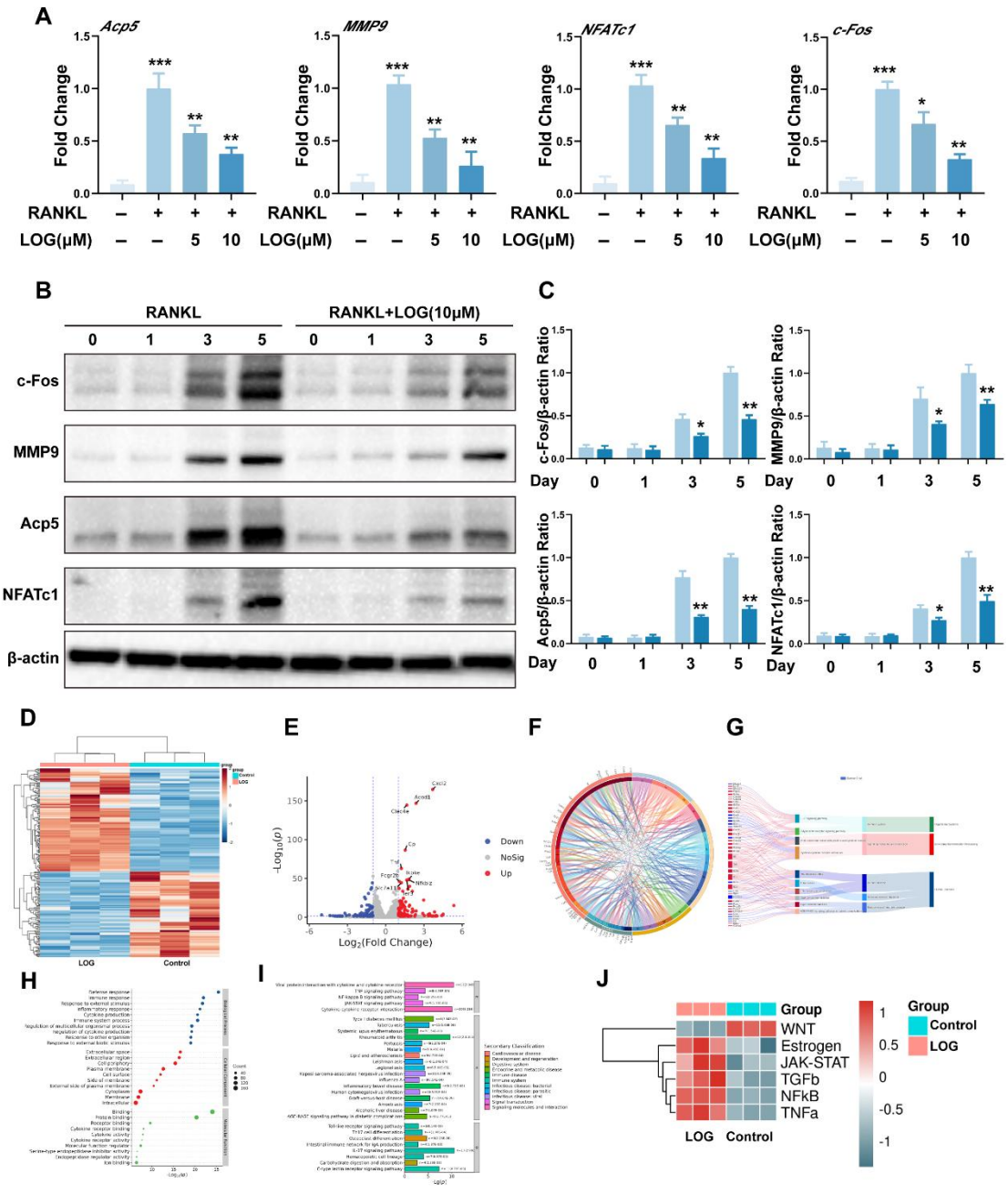

A
Acp5
MMP9
NFATc1
c-Fos
Fold Change
RANKL
LOG(μM)
B
RANKL
RANKL+LOG(10μM)
c-Fos
MMP9
Acp5
NFATc1
β-actin
C
c-Fos/β-actin Ratio
MMP9/β-actin Ratio
Acp5/β-actin Ratio
NFATc1/β-actin Ratio
Day
D
LOG
Control
E
Down
NoSig
Up
F
G
H
I
J
Group
WNT
Estrogen
JAK-STAT
TGFb
NFkB
TNFa
Control
LOG

Figure 3 :

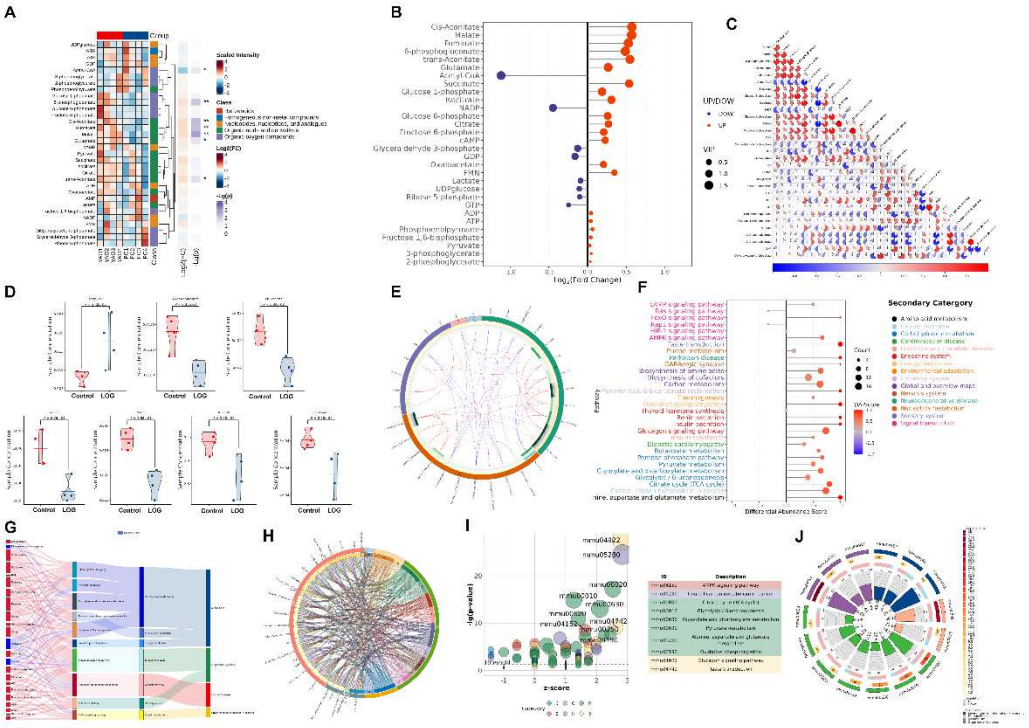


Figure 4 :

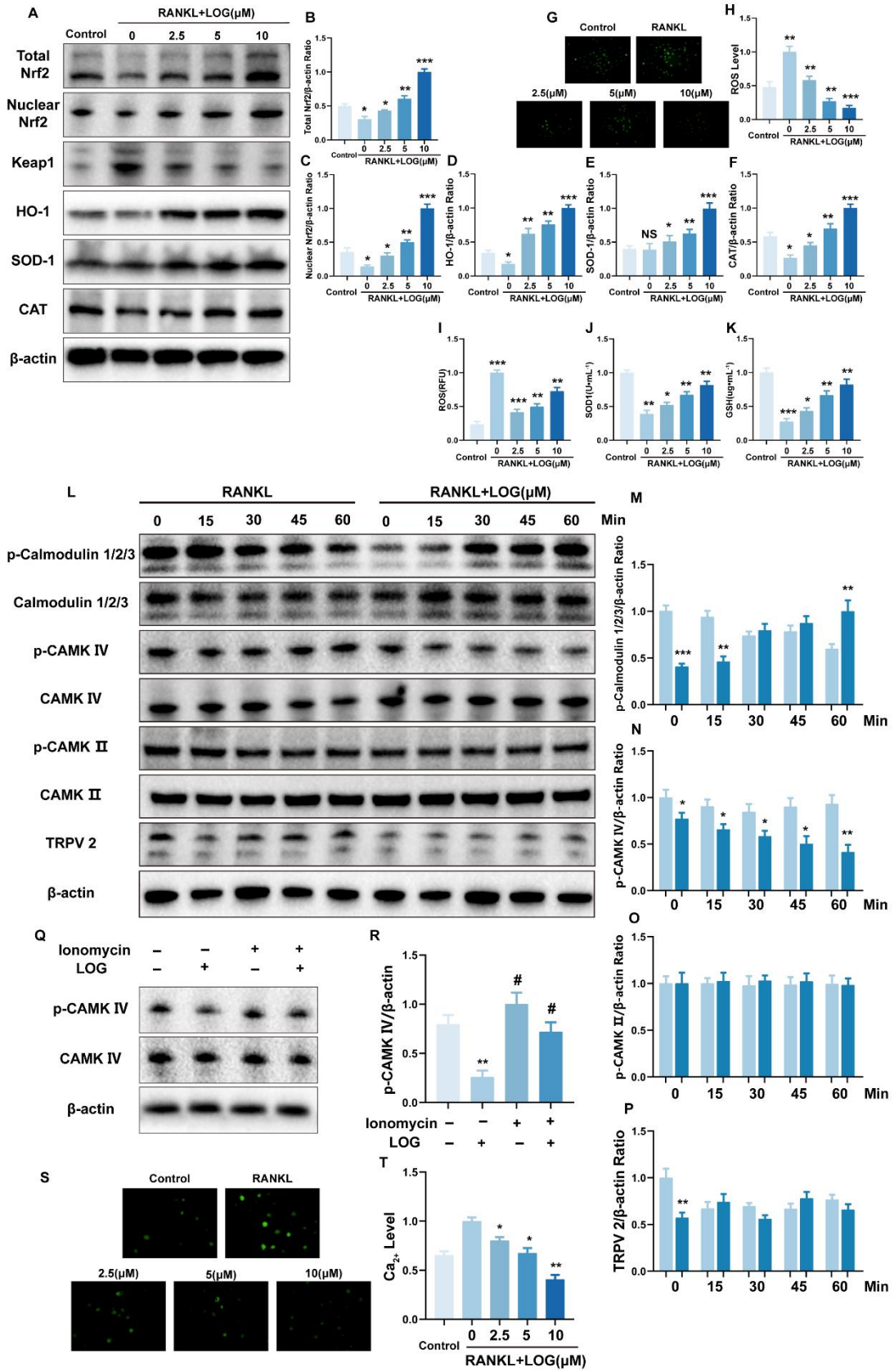

A
RANKL+LOG(μM)
Control
0
2.5
5
10
Total Nrf2
Nuclear Nrf2
Keap1
HO-1
SOD-1
CAT
β-actin
B
Total Nrf2/β-actin Ratio
C
Nuclear Nrf2/β-actin Ratio
D
HO-1/β-actin Ratio
E
SOD-1/β-actin Ratio
NS
F
CAT/β-actin Ratio
G
Control
RANKL
2.5(μM)
5(μM)
10(μM)
H
ROS Level
I
ROS(RFU)
J
SOD1(U·mL⁻¹)
K
GSH(ug·mL⁻¹)
L
RANKL
RANKL+LOG(μM)
0
15
30
45
60
Min
p-Calmodulin 1/2/3
Calmodulin 1/2/3
p-CAMK Ⅳ
CAMK Ⅳ
p-CAMK Ⅱ
CAMK Ⅱ
TRPV 2
β-actin
M
p-Calmodulin 1/2/3/β-actin Ratio
N
p-CAMK Ⅳ/β-actin Ratio
O
p-CAMK Ⅱ/β-actin Ratio
P
TRPV 2/β-actin Ratio
Q
Ionomycin
LOG
p-CAMK Ⅳ
CAMK Ⅳ
β-actin
R
p-CAMK Ⅳ/β-actin
S
Control
RANKL
2.5(μM)
5(μM)
10(μM)
T
Ca2+ Level

Figure 5 :

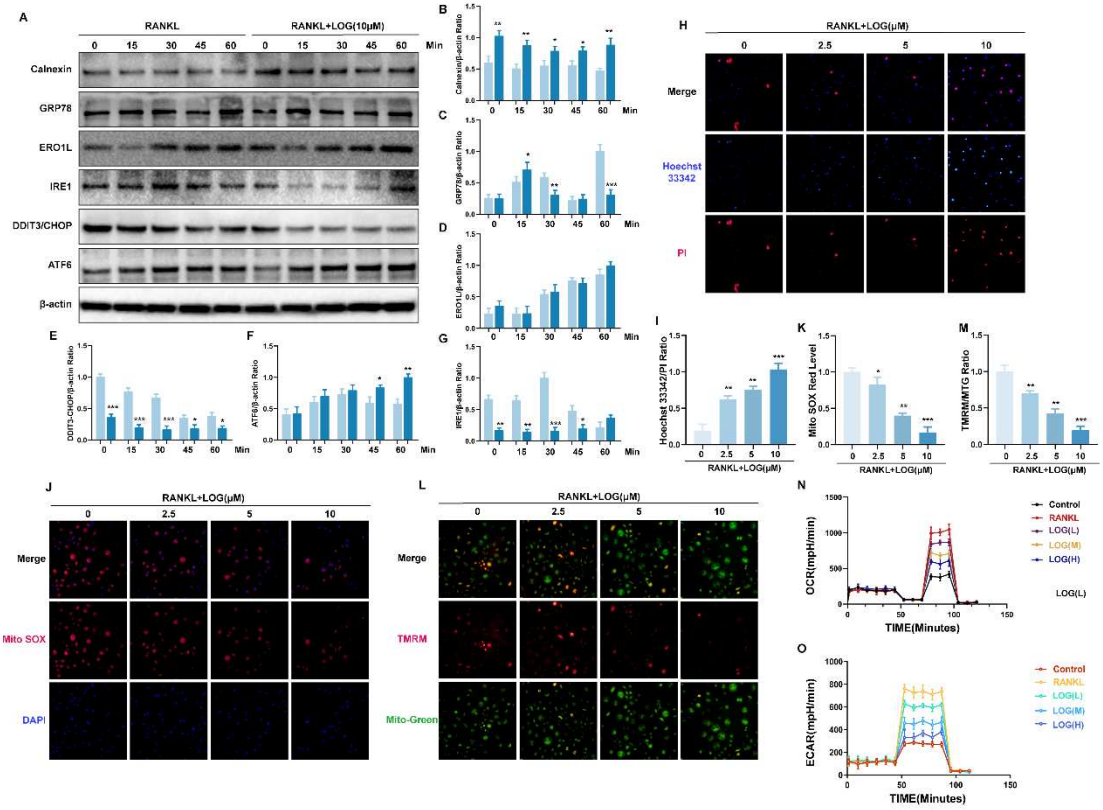

A
RANKL
RANKL+LOG(10μM)
0 15 30 45 60 0 15 30 45 60 Min
Calnexin
GRP78
ERO1L
IRE1
DDIT3/CHOP
ATF6
β-actin
B
Calnexin/β-actin Ratio
C
GRP78/β-actin Ratio
D
ERO1L/β-actin Ratio
E
DDIT3-CHOP/β-actin Ratio
F
ATF6/β-actin Ratio
G
IRE1/β-actin Ratio
H
RANKL+LOG(μM)
0 2.5 5 10
Merge
Hoechst 33342
PI
I
Hoechst 33342/PI Ratio
K
Mito SOX Red Level
M
TMRM/MTG Ratio
J
RANKL+LOG(μM)
Merge
Mito SOX
DAPI
L
RANKL+LOG(μM)
Merge
TMRM
Mito-Green
N
OCR(mpH/min)
TIME(Minutes)
Control
RANKL
LOG(L)
LOG(M)
LOG(H)
LOG(L)
O
ECAR(mpH/min)
TIME(Minutes)
Control
RANKL
LOG(L)
LOG(M)
LOG(H)

Figure 6 :

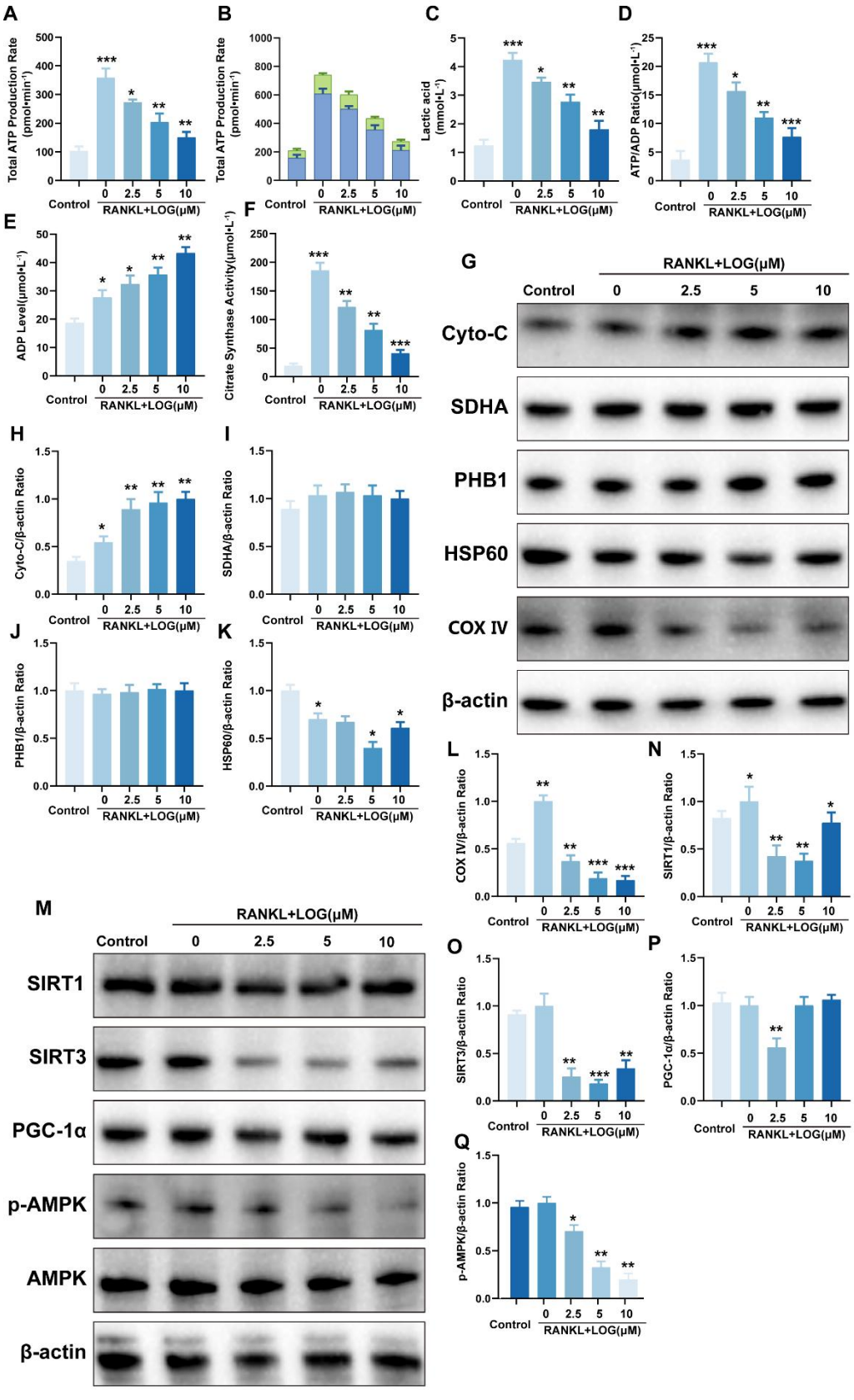

A
Total ATP Production Rate (pmol•min⁻¹)
B
Total ATP Production Rate (pmol•min⁻¹)
C
Lactic acid (mmol•L⁻¹)
D
ATP/ADP Ratio(μmol•L⁻¹)
E
ADP Level(μmol•L⁻¹)
F
Citrate Synthase Activity(μmol•L⁻¹)
G
RANKL+LOG(μM)
Control
0
2.5
5
10
Cyto-C
SDHA
PHB1
HSP60
COX Ⅳ
β-actin
H
Cyto-C/β-actin Ratio
I
SDHA/β-actin Ratio
J
PHB1/β-actin Ratio
K
HSP60/β-actin Ratio
L
COX Ⅳ/β-actin Ratio
N
SIRT1/β-actin Ratio
M
SIRT1
SIRT3
PGC-1α
p-AMPK
AMPK
β-actin
O
SIRT3/β-actin Ratio
P
PGC-1α/β-actin Ratio
Q
p-AMPK/β-actin Ratio

Figure 6 :

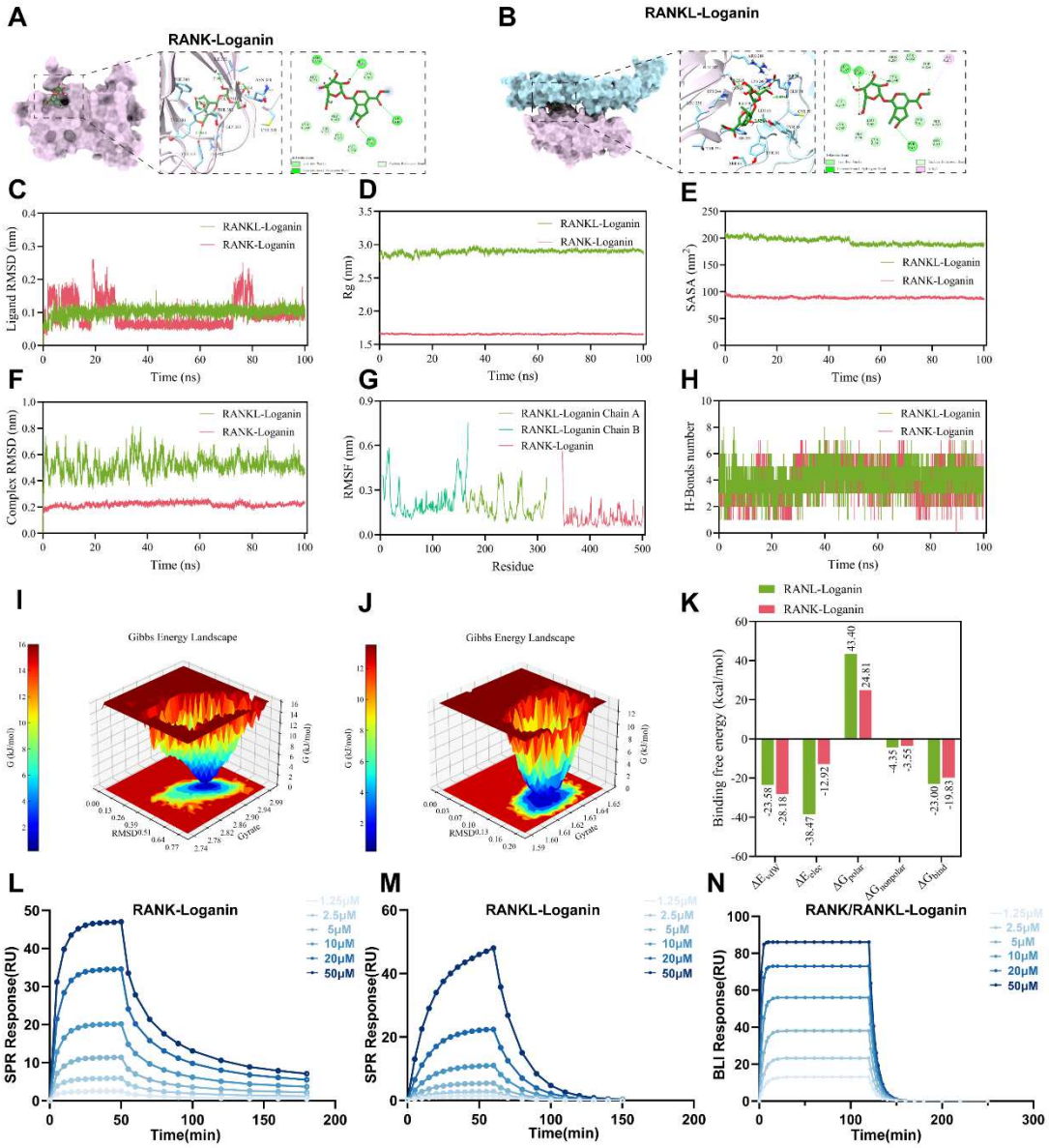

A
RANK-Loganin
B
RANKL-Loganin
C
RANKL-Loganin
RANK-Loganin
Ligand RMSD (nm)
Time (ns)
D
RANKL-Loganin
RANK-Loganin
Rg (nm)
Time (ns)
E
RANKL-Loganin
RANK-Loganin
SASA (nm²)
Time (ns)
F
RANKL-Loganin
RANK-Loganin
Complex RMSD (nm)
Time (ns)
G
RANKL-Loganin Chain A
RANKL-Loganin Chain B
RANK-Loganin
RMSF (nm)
Residue
H
RANKL-Loganin
RANK-Loganin
H-Bonds number
Time (ns)
I
Gibbs Energy Landscape
J
Gibbs Energy Landscape
K
RANL-Loganin
RANK-Loganin
Binding free energy (kcal/mol)
-23.58
-28.18
-38.47
-12.92
43.40
24.81
-4.35
-3.55
-23.00
-19.83
L
RANK-Loganin
SPR Response(RU)
Time(min)
1.25μM
2.5μM
5μM
10μM
20μM
50μM
M
RANKL-Loganin
SPR Response(RU)
Time(min)
N
RANK/RANKL-Loganin
BLI Response(RU)
Time(min)

Figure 7 :

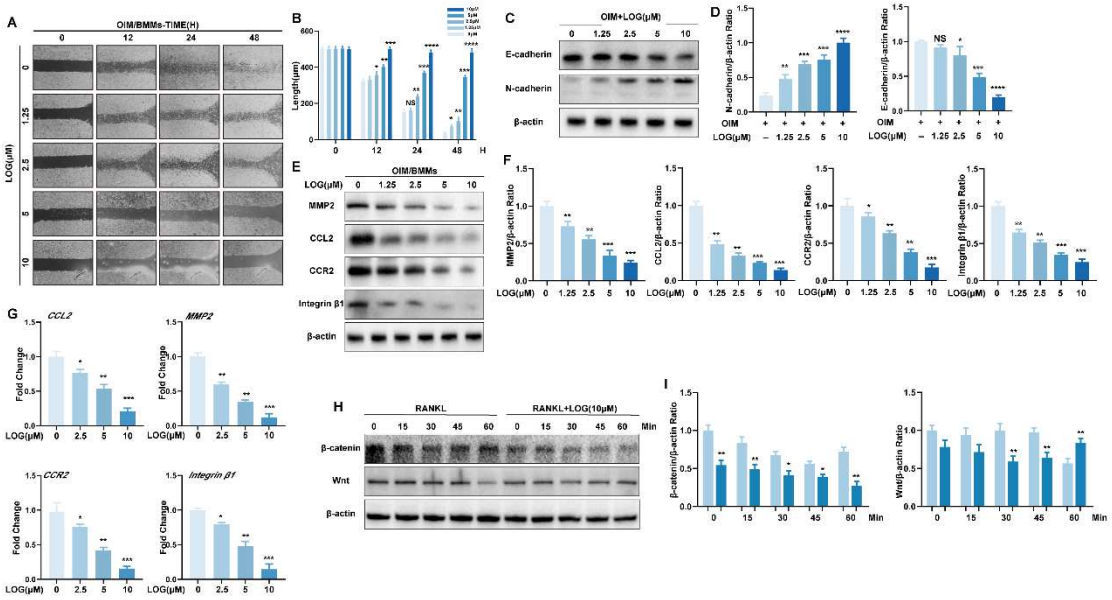

A
OIM/BMMs-TiME(H)
0
12
24
48
LOG(μM)
0
1.25
2.5
5
10
B
Length(μm)
NS
H
C
OIM+LOG(μM)
E-cadherin
N-cadherin
β-actin
D
N-cadherin/β-actin Ratio
E-cadherin/β-actin Ratio
NS
OIM
LOG(μM)
E
OIM/BMMs
MMP2
CCL2
CCR2
Integrin β1
β-actin
F
MMP2/β-actin Ratio
CCL2/β-actin Ratio
CCR2/β-actin Ratio
Integrin β1/β-actin Ratio
G
CCL2
MMP2
CCR2
Integrin β1
Fold Change
H
RANKL
RANKL+LOG(10μM)
Min
β-catenin
Wnt
β-actin
I
β-catenin/β-actin Ratio
Wnt/β-actin Ratio

Figure 8 :

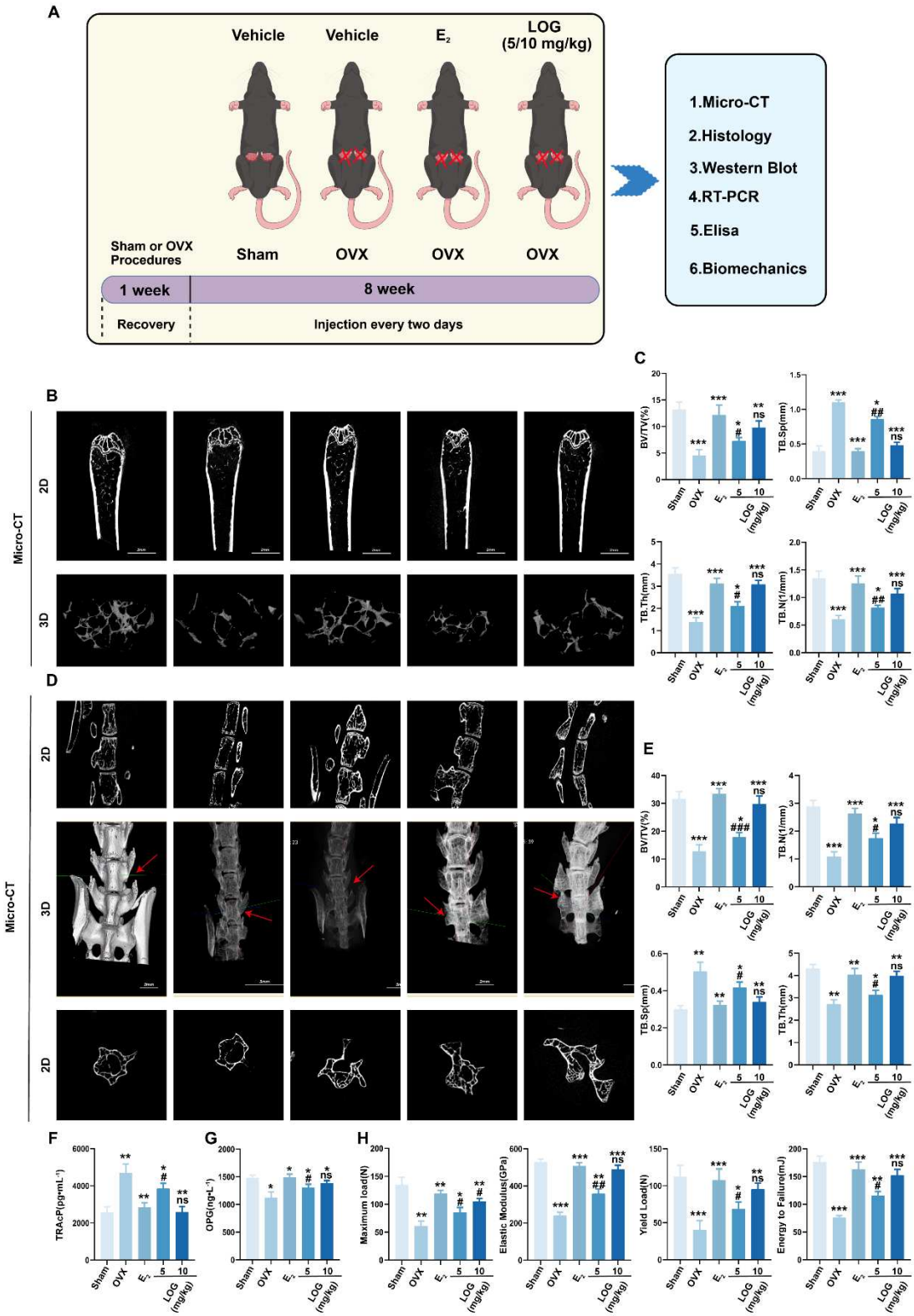

A
Vehicle
Vehicle
E2
LOG (5/10 mg/kg)
Sham or OVX Procedures
Sham
OVX
OVX
OVX
1 week
8 week
Recovery
Injection every two days
1.Micro-CT
2.Histology
3.Western Blot
4.RT-PCR
5.Elisa
6.Biomechanics
B
C
D
E
F
G
H
Micro-CT
2D
3D
BV/TV(%)
TB.Sp(mm)
TB.Th(mm)
TB.N(1/mm)
TRACP(pg·mL⁻¹)
OPG(ng·L⁻¹)
Maximum load(N)
Elastic Modulus(GPa)
Yield Load(N)
Energy to Failure(mJ)
Sham
OVX
E2
5
10
LOG (mg/kg)

Figure 9 :

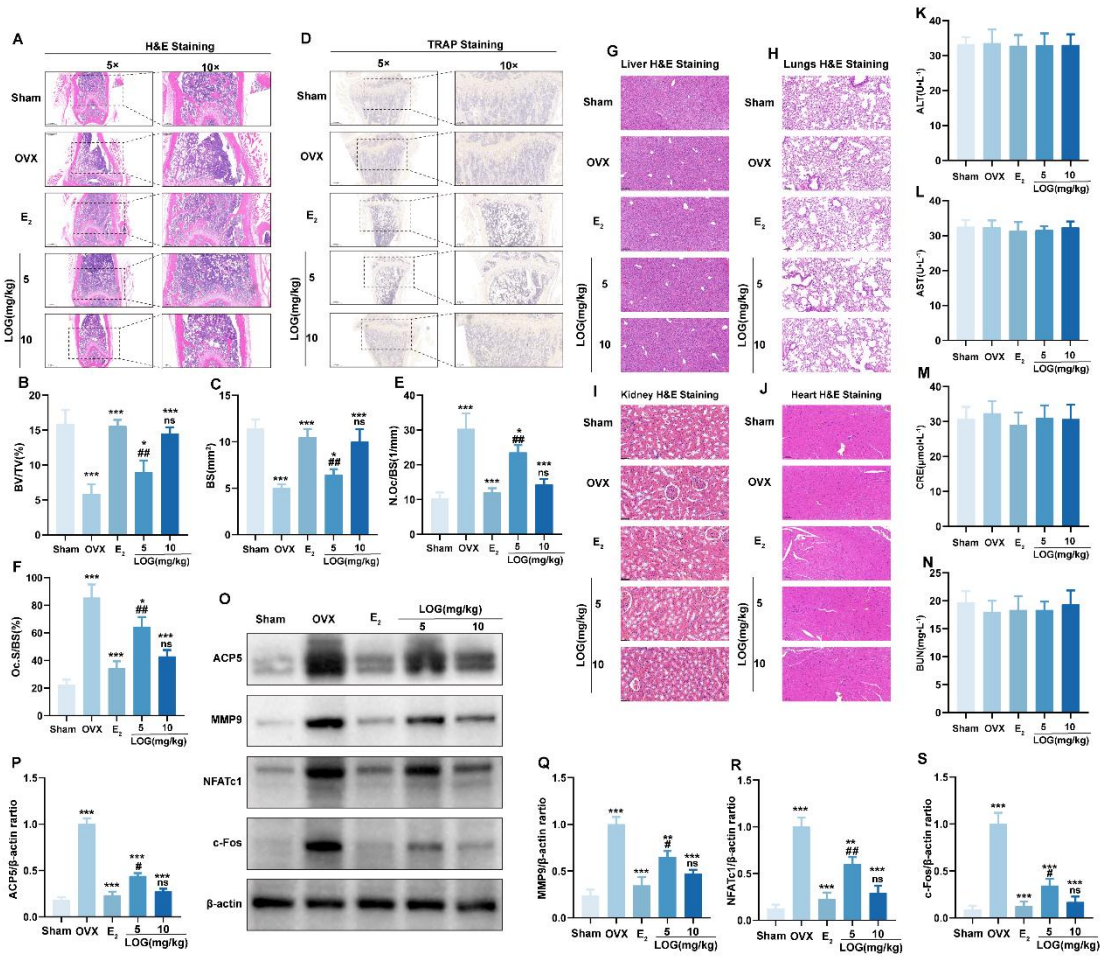
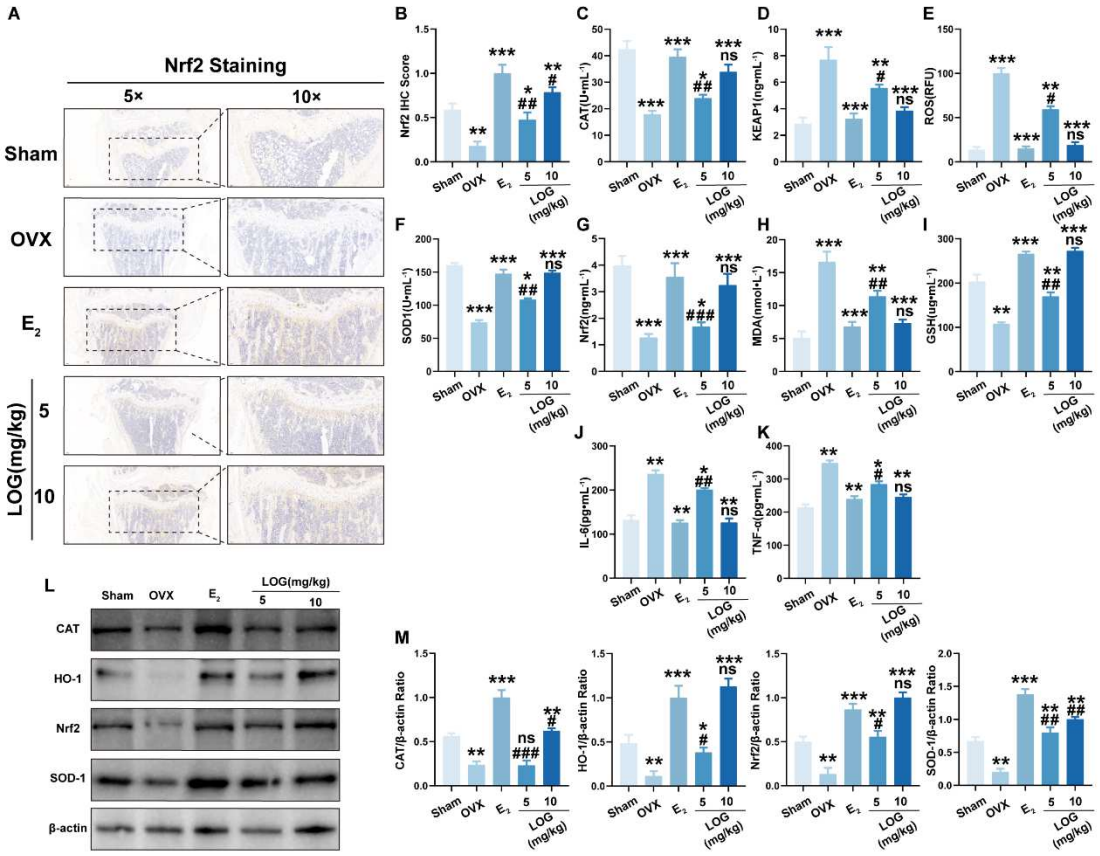

A
H&E Staining
5×
10×
Sham
OVX
E2
LOG(mg/kg)
5
10
D
TRAP Staining
G
Liver H&E Staining
H
Lungs H&E Staining
I
Kidney H&E Staining
J
Heart H&E Staining
B
BV/TV(%)
C
BS(mm²)
E
N.Oc/BS(1/mm)
F
Oc.S/BS(%)
O
ACP5
MMP9
NFATc1
c-Fos
β-actin
P
ACP5/β-actin ratio
Q
MMP9/β-actin ratio
R
NFATc1/β-actin ratio
S
c-Fos/β-actin ratio
K
ALT(U/L⁻¹)
L
AST(U/L⁻¹)
M
CRE(μmol·L⁻¹)
N
BUN(mg·L⁻¹)

Figure 10 :


A
Nrf2 Staining
5×
10×
Sham
OVX
E2
LOG(mg/kg)
5
10
B
Nrf2 IHC Score
C
CAT(U·mL-1)
D
KEAP1(ng·mL-1)
E
ROS(RFU)
F
SOD1(U·mL-1)
G
Nrf2(ng·mL-1)
H
MDA(nmol·L-1)
I
GSH(ug·mL-1)
J
IL-6(pg·mL-1)
K
TNF-α(pg·mL-1)
L
Sham
OVX
E2
LOG(mg/kg)
5
10
CAT
HO-1
Nrf2
SOD-1
β-actin
M
CAT/β-actin Ratio
HO-1/β-actin Ratio
Nrf2/β-actin Ratio
SOD-1/β-actin Ratio
LOG (mg/kg)

References:

Boyce, B.F., Xing, L., 2008. Functions of RANKL/RANK/OPG in bone modeling and remodeling. Arch Biochem Biophys 473(2), 139-146.

Chen, S., Long, Y., Guo, Z., Di, J., Xu, J., Xiang, C., 2025. Pathophysiological Insights Into the Role of Osteoclasts in Osteoarthritis: Mechanisms, Therapeutic Targets, and Future Directions. J Inflamm Res 18(11191-11204.

Chen, Y., Chen, J., Jiang, M., Fu, Y., Zhu, Y., Jiao, N., Liu, L., Du, Q., Wu, H., Xu, H., Sun, J., 2020. Loganin and catalpol exert cooperative ameliorating effects on podocyte apoptosis upon diabetic nephropathy by targeting AGEs-RAGE signaling. Life Sci 252(117653.

Compston, J.E., McClung, M.R., Leslie, W.D., 2019. Osteoporosis. Lancet 393(10169), 364-376.

Da, W., Tao, L., Zhu, Y., 2021. The Role of Osteoclast Energy Metabolism in the Occurrence and Development of Osteoporosis. Front Endocrinol (Lausanne) 12(675385.

Deng, W., Liu, Y., Guo, Y., Chen, J., Abdu, H.I., Khan, M.R.U., Palanisamy, C.P., Pei, J., Abd El-Aty, A.M., 2023. A comprehensive review of Cornus officinalis: health benefits, phytochemistry, and pharmacological effects for functional drug and food development. Front Nutr 10(1309963.

Dong, Y., Feng, Z.L., Chen, H.B., Wang, F.S., Lu, J.H., 2018. Corni Fructus: a review of chemical constituents and pharmacological activities. Chin Med 13(34.

Flanigan, J., Kane, S., Mirzayeh Fashami, F., Zhou, A., Almuallem, L., Tindal, M., Schauf, M., Li, E., Lyman, G.H., 2026. Cost-Effectiveness of Biosimilar Denosumab Versus Bisphosphonates in Postmenopausal Osteoporosis. Pharmacoecon Open.

Green, C.D., Maceyka, M., Cowart, L.A., Spiegel, S., 2021. Sphingolipids in metabolic disease: The good, the bad, and the unknown. Cell Metab 33(7), 1293-1306.

Kanis, J.A., Norton, N., Harvey, N.C., Jacobson, T., Johansson, H., Lorentzon, M., McCloskey, E.V., Willers, C., Borgstrom, F., 2021. SCOPE 2021: a new scorecard for osteoporosis in Europe. Arch Osteoporos 16(1), 82.

Lee, C.G., Kim, D.W., Kim, J., Uprety, L.P., Oh, K.I., Singh, S., Yoo, J., Jin, H.S., Choi, T.H., Park, E., Jeong, S.Y., 2022. Effects of Loganin on Bone Formation and Resorption In Vitro and In Vivo. Int J Mol Sci 23(22).

Lemma, S., Sboarina, M., Porporato, P.E., Zini, N., Sonveaux, P., Di Pompo, G., Baldini, N., Avnet, S., 2016. Energy metabolism in osteoclast formation and activity. Int J Biochem Cell Biol 79(168-180.

Li, J., Zhang, L., Peng, J., Zhao, C., Li, W., Yu, Y., Huang, X., Yang, F., Deng, X., Yang, X., Zhang, T., Peng, J., 2025. Mitochondrial metabolic regulation of macrophage polarization in osteomyelitis and other orthopedic disorders: mechanisms and therapeutic opportunities. Front Cell Dev Biol 13(1604320.

Liu, Q., Zhao, A., Wu, X., Zhang, X., Li, X., Yang, W., Lei, W., Liu, H., Zhao, H., Jiang, S., Yang, Y., Shen, M., 2024. Identifying and validating potential therapeutic targets for septic heart failure and the cardioprotective effects of lycorine. Phytomedicine 129(155677.

Long, Z.Y., Wu, J.M., Xiang, W., Yuan, M.X., Wu, Y.H., Li, J., Yu, G.P., Yang, T., 2022.

Research on the Mechanism of Liuwei Dihuang Decoction for Osteoporosis Based on Systematic Biological Strategies. Evid Based Complement Alternat Med 2022(7017610.
McDonald, M.M., Kim, A.S., Mulholland, B.S., Rauner, M., 2021. New Insights Into Osteoclast Biology. JBMR Plus 5(9), e10539.
Misra, A., Chaudhary, M.K., Tripathi, D., Srivastava, P.K., Gupta, V., Acharya, R., Srivastava, S., 2023. Nutritional potential of an edible terrestrial orchid Eulophia nuda LINDL and validation of its traditional claim in arthritis. J Ethnopharmacol 306(116123.
Novotortsev, V.K., Kukushkin, M.E., Tafeenko, V.A., Skvortsov, D.A., Kalinina, M.A., Timoshenko, R.V., Chmelyuk, N.S., Vasilyeva, L.A., Tarasevich, B.N., Gorelkin, P.V., Erofeev, A.S., Majouga, A.G., Zyk, N.V., Beloglazkina, E.K., 2021. Dispirooxindoles Based on 2-Selenoxo-Imidazolidin-4-Ones: Synthesis, Cytotoxicity and ROS Generation Ability. Int J Mol Sci 22(5).
Ono, T., Hayashi, M., Sasaki, F., Nakashima, T., 2020. RANKL biology: bone metabolism, the immune system, and beyond. Inflamm Regen 40(2.
Park-Min, K.H., 2019. Metabolic reprogramming in osteoclasts. Semin Immunopathol 41(5), 565-572.
Park, J.H., Lee, N.K., Lee, S.Y., 2017. Current Understanding of RANK Signaling in Osteoclast Differentiation and Maturation. Mol Cells 40(10), 706-713.
Pereira, M., Petretto, E., Gordon, S., Bassett, J.H.D., Williams, G.R., Behmoaras, J., 2018. Common signalling pathways in macrophage and osteoclast multinucleation. J Cell Sci 131(11).
Ren, S., Zhou, Y., Zheng, K., Xu, X., Yang, J., Wang, X., Miao, L., Wei, H., Xu, Y., 2022. Cerium oxide nanoparticles loaded nanofibrous membranes promote bone regeneration for periodontal tissue engineering. Bioact Mater 7(242-253.
Salari, N., Ghasemi, H., Mohammadi, L., Behzadi, M.H., Rabieenia, E., Shohaimi, S., Mohammadi, M., 2021. The global prevalence of osteoporosis in the world: a comprehensive systematic review and meta-analysis. J Orthop Surg Res 16(1), 609.
Sun, Y., Li, J., Xie, X., Gu, F., Sui, Z., Zhang, K., Yu, T., 2021. Macrophage-Osteoclast Associations: Origin, Polarization, and Subgroups. Front Immunol 12(778078.
Tang, Q., Ke, H., Wu, C., Zeng, J., Li, Z., Liu, Y., Feng, S., Xue, Q., Xu, X., 2019. Aqueous extract from You-Gui-Yin ameliorates cognitive impairment of chronic renal failure mice through targeting hippocampal CaMKIIalpha/CREB/BDNF and EPO/EPOR pathways. J Ethnopharmacol 239(111925.
Wang, R., Zhang, W., Ma, H., Zou, D., Zhang, Z., Wang, S., 2022. Structural insights into the binding of zoledronic acid with RANKL via computational simulations. Front Mol Biosci 9(992473.
Xu, Y., An, Z., Hou, K., Zhou, M., Liu, Y., Wang, J., Hashimoto, M., Wei, J., 2025. ACE2 Alleviates Microglia Neuroinflammation by RANK-RANKL-OPG Axis in Parkinson's Disease. Inflammation 48(6), 4364-4378.
Zhang, T., Ding, S., Wang, R., 2021. Research Progress of Mitochondrial Mechanism in NLRP3 Inflammasome Activation and Exercise Regulation of NLRP3 Inflammasome. Int J Mol Sci 22(19).
Zhao, W., Deng, W., Wang, Y., Zhu, R., Liu, J., Chen, H., Tang, W., Luo, Y., Du, A., Zhu, H.,

Sun, M., Shen, G., Ren, H., Luan, J., Jiang, X., Yi, S., 2026. Liquiritigenin suppresses osteoclastogenesis via multi-target mechanisms involving NF-kappaB/PI3K-AKT signaling pathways and metabolic reprogramming. Biochem Pharmacol 246(117678.

Zhou, B., Zhang, Y., Yu, W., Sun, L., Wang, Y., Jiang, Y., Wang, O., Xing, X., Xia, W., Zhang, J., Yan, W., Li, M., 2026a. Efficacy and safety of denosumab, zoledronic acid and alendronate on bone mineral density and trabecular bone score in men with osteoporosis. Age Ageing 55(5).

Zhou, J., Ma, Z., Ding, Y., Yan, X., Tan, Q., 2026b. Loganin promotes diabetic wound healing and inhibits NLRP3 inflammasomes in diabetic mice via IL17/NF-kappaB signaling. Int Immunopharmacol 181(116767.

Supplementary Files

This is a list of supplementary files associated with this preprint. Click to download.

- SupplementaryTableS1.docx
- SupplementaryTableS2..docx